

ON A CLASS OF MULTI-FIDELITY METHODS FOR THE SEMICLASSICAL SCHRÖDINGER EQUATION WITH UNCERTAINTIES*

YIWEN LIN[†] AND LIU LIU[‡]

Abstract. In this paper, we study the semiclassical Schrödinger equation with random parameters and develop several robust multi-fidelity methods. We employ the time-splitting Fourier pseudospectral (TSFP) method for the high-fidelity solver, and consider different low-fidelity solvers including the meshless method like frozen Gaussian approximation (FGA) and the level set (LS) method for the semiclassical limit of the Schrödinger equation. With a careful choice of the low-fidelity model, we obtain an error estimate for the bi-fidelity method. We conduct numerous numerical experiments and validate the accuracy and efficiency of our proposed multi-fidelity methods, by comparing the performance of a class of bi-fidelity and tri-fidelity approximations.

Key words. Schrödinger equation, uncertainty quantification, multi-fidelity method, error estimate

MSC codes. 35J10, 65M70

1. Introduction. Uncertainty Quantification (UQ) has drawn an increasing attention over the last decades. The study of UQ involves quantitative characterization and management of uncertainties in the inputs of models, which is important to assess, validate and improve these models, then to produce more reliable predictions for the outputs.

In UQ, the nonintrusive stochastic collocation (SC) method has been popularly used. One key challenge to collocation approaches is the computational cost, as it requires repetitive implementations of the deterministic solver, especially for complex problems or high-dimensional random uncertainties, thus makes the simulation difficult or infeasible. There have been many study in this direction, for example [1, 6, 23, 24, 28]. Fortunately, there usually exist some approximated, less complicated low-fidelity models in practice. Compared to the high-fidelity models, these low-fidelity models usually contain simplified physics or are simulated on a coarser mesh in physical space. The goal of multi-fidelity algorithm in the SC framework is to combine the computation efficiency of low-fidelity models with the high accuracy of high-fidelity models, thus can construct an accurate surrogate for the high-fidelity model and produce reliable results, at a significantly reduced simulation cost. Regarding UQ for kinetic equations and related problems with random inputs, there is a review article [25] focused on some of the recent progress on multi-fidelity methods for kinetic equations.

Compared to bi-fidelity methods, the tri-fidelity method can be more accurate and more efficient. The reasons are the following: if we consider three solvers ($U^{(1)}$, $U^{(2)}$, $U^{(3)}$), fixing $U^{(3)}$ as the high-fidelity solver, one has two options of the bi-

*Submitted to the editors May 22, 2024.

Funding: L. Liu acknowledges the support by National Key R&D Program of China (2021YFA1001200), Ministry of Science and Technology in China, Early Career Scheme (24301021) and General Research Fund (14303022 & 14301423) funded by Research Grants Council of Hong Kong from 2021-2023. Y. Lin was partially supported by National Natural Science Foundation of China (12201404) and China Postdoctoral Science Foundation (2021TQ0203).

[†]School of Mathematical Sciences and Institute of Natural Sciences, Shanghai Jiao Tong University, Shanghai 200240, P.R. China (linyiw@sjtu.edu.cn).

[‡]The Chinese University of Hong Kong, Hong Kong (liu@math.cuhk.edu.hk).

fidelity method B_I and B_{II} , with $U^{(1)}$ and $U^{(2)}$ chosen as the low-fidelity solver respectively. For the tri-fidelity method, if $\|U^{(3)} - U^{(2)}\| \leq \|U^{(3)} - U^{(1)}\|$ under some appropriate norm to be specified later, one can conclude that the tri-fidelity method is more accurate than the bi-fidelity method B_I ; on the other hand, if $U^{(1)}$ is much cheaper than $U^{(2)}$, the point selection procedure that uses $U^{(1)}$ instead of $U^{(2)}$ in the tri-fidelity method will be faster than that in the bi-fidelity method B_{II} , thus the tri-fidelity method can be faster than B_{II} . Therefore developing tri-fidelity methods is a necessary and timely task.

In this paper, we consider the dimensionless Schrödinger equation with random initial data and potential function:

$$(1.1) \quad \begin{cases} i\varepsilon\partial_t\psi = -\frac{\varepsilon^2}{2}\partial_{xx}\psi + V(x, z)\psi, & t > 0, x \in \Omega, \\ \psi(t, x, z) = \psi_0(x, z), \end{cases}$$

where $\Omega = (a, b) \in \mathbb{R}$ is a bounded domain equipped with periodic boundary conditions. The parameter ε , named the semiclassical parameter, describes the microscopic macroscopic scale ratio and is small within the semiclassical regime (i.e. $0 < \varepsilon \ll 1$). From $\psi(t, x, z) \in \mathbb{C}$, one can compute the physical quantities including position density and current density:

$$\rho^\varepsilon(t, x, z) = |\psi^\varepsilon(t, x, z)|^2, \quad J^\varepsilon(t, x, z) = \varepsilon \operatorname{Im} \left(\overline{\psi^\varepsilon(t, x, z)} \nabla \psi^\varepsilon(t, x, z) \right),$$

where “ $\bar{}$ ” denotes complex conjugation.

For the high-fidelity solver, we utilize the time-splitting Fourier pseudospectral (TSFP) method [3, 4] in this paper. Note that if one uses the stochastic collocation (SC) method for TSFP, the number of collocation points should be $O(1/\varepsilon)$ [13]. It motivates us to develop a class of multi-fidelity method for the Schrödinger equation with uncertainties. From numerical tests in Section 4.1, we find that our multi-fidelity method is more efficient than the SC method for TSFP, when achieving the same level of accuracy. In order to explore cheaper solvers for the low-fidelity models to significantly reduce the computational cost for the Schrödinger equation with random inputs, in this paper we investigate the bi- and tri-fidelity methods for (1.1). In particular, the frozen Gaussian approximation (FGA) [19], and level set (LS) method [12] for the semi-classical limit of the Schrödinger equation are utilized. Since FGA outperforms the existing algorithms in that it is mesh-free in computing the physical observables and is suitable for high dimensional problems, we will employ the FGA as one choice of the low-fidelity solver for (1.1). Through comparing different choices of low-fidelity solvers in the bi-fidelity method as well as implementing the tri-fidelity method, we examine the performance of the proposed methods, and give some insights on choices of the low-fidelity and medium-fidelity methods. Since one needs to explore the random space spanned by the low-fidelity solutions by repeatedly running the low-fidelity solvers N times (with N significantly large), thus the relatively cheaper solver is chosen as the low-fidelity model, compared with medium- and high-fidelity solvers. Between the medium- and high-fidelity solvers, we tend to choose the more accurate one as the high-fidelity solver. As for the analysis, we establish an error estimate of the bi-fidelity method for the semiclassical Schrödinger equation (1.1) with random parameters, with FGA and TSFP scheme for the low- and high-fidelity solvers.

This paper is organized as follows. Section 2 gives an introduction to several solvers for the Schrödinger equation as well as its semiclassical limit. Section 3 is

dedicated to establishing an error estimate of the bi-fidelity method. In Section 4, we compare bi-fidelity methods with different choices of low-fidelity solvers and present numerical results for both bi- and tri-fidelity methods. Conclusions are shown in Section 5.

2. Multi-fidelity method. Below is a summary of the bi-fidelity algorithm [31]. Our sought bi-fidelity approximation of u^H is constructed by

$$\mathbf{U}^B(z) = \sum_{k=1}^K c_k^L(z) \mathbf{U}^H(z_k).$$

In the offline stage, one employs the cheap low-fidelity model to select the most important parameter points $\{\gamma_K\}$ by the greedy procedure [8]. In the online stage, for any sample point $z \in I_z$, we project the low-fidelity solution $\mathbf{U}^L(z)$ onto the low-fidelity approximation space $\mathcal{U}^L(\gamma_K)$:

$$\mathbf{U}^L(z) \approx \mathcal{P}_{\mathcal{U}^L(\gamma_K)}[\mathbf{U}^L(z)] = \sum_{k=1}^K c_k^L(z) \mathbf{U}^L(z_k),$$

where $\mathcal{P}_{\mathcal{U}^L(\gamma_K)}$ is the projection operator onto $\mathcal{U}^L(\gamma_K)$ with projection coefficients $\{c_k\}$ computed by the Galerkin approach: $\mathbf{G}^L \mathbf{c} = \mathbf{f}$, where $\mathbf{f} = (f_k)_{1 \leq k \leq K}$ with $f_k = \langle \mathbf{U}^L(z), \mathbf{U}^L(z_k) \rangle^L$, and \mathbf{G}^L is the Gramian matrix for $\mathcal{U}^L(\gamma_K)$. The bi-fidelity algorithm is given in Algorithm 2.1. We propose to extend the research in this direction.

In many practical problems, there may exist more than two models, each with a different fidelity and simulation cost. Thus multi-fidelity approximation [22, 31] has developed recently. As proposed in [31], for the tri-fidelity model, the key is to use the low-fidelity model to select the “important” subset γ_K out of the dense point set Γ_N . Then the medium-fidelity model is used to construct the approximation rule. Compared to the high-fidelity model \mathbf{U}^H , the medium-fidelity model \mathbf{U}^M is cheaper to simulate. Compared to the low-fidelity model \mathbf{U}^L , \mathbf{U}^M offers better accuracy, yet it is more expensive and cannot be simulated over the dense point set Γ_N . The tri-fidelity algorithm is described in Algorithm 2.2. If there exists more than three models for the investigated problem, there always exists a tri-fidelity model by choosing the appropriate high-, low- and medium-fidelity models.

In this paper, we will always employ the time-splitting Fourier pseudospectral (TSFP) method as the high-fidelity method, the frozen Gaussian approximation (FGA) as one choice of the low-fidelity solvers and level set (LS) method as another choice of the low-fidelity solvers. For the rest of this section, we will give a brief introduction of these solvers.

2.1. The high-fidelity TSFP method. In this section, we will introduce our choice of the high-fidelity solver for solving the Schrödinger equation (1.1), namely the time-splitting Fourier pseudospectral (TSFP) method [4]. First we mention some existing numerical schemes for the deterministic Schrödinger equation.

Due to the highly oscillatory structure of the wave function, various effective numerical algorithms have been proposed and developed. Traditional algorithms can be divided into two classes: direct discretization methods and asymptotic methods. Popular choices of direct discretization methods include finite difference time domain method, the time-splitting spectral method (TSSP) [5] and time-splitting Fourier pseudospectral (TSFP) method [3, 4]. In [5], the authors gave an error estimate in L^2 norm for the time splitting spectral method and recently [4] established an improved

Algorithm 2.1 Bi-fidelity approximation for a high-fidelity solution at given z

Offline:

- 1 Select a sample set $\Gamma_N = \{z_1, z_2, \dots, z_N\} \subset I_z$.
- 2 Run the low-fidelity model $\mathbf{U}^L(z_j)$ for each $z_j \in \Gamma_N$.
- 3 Select K “important” points from Γ_N . Denote $\gamma_K = \{z_{i_1}, \dots, z_{i_K}\} \subset \Gamma_N$. Construct the low-fidelity approximation space $\mathcal{U}^L(\gamma_K)$.
- 4 Run high-fidelity simulation at each sample point in the selected sample set γ_K . Construct the high-fidelity approximation space $\mathcal{U}^H(\gamma_K)$.

Online:

- 5 For any given z , compute the low-fidelity solution $\mathbf{U}^L(z)$ and the corresponding low-fidelity coefficients by projection:

$$(2.1) \quad \mathbf{U}^L(z) \approx \mathcal{P}_{\mathcal{U}^L(\gamma_K)} \left[\mathbf{U}^L(z) \right] = \sum_{k=1}^K c_k^L(z) \mathbf{U}^L(z_k), \quad z_k \in \gamma_K.$$

The operator $\mathcal{P}_{\mathcal{U}^L(\gamma_K)}$ in (2.1) is a projection onto the space $\mathcal{U}^L(\gamma_K)$ with projection coefficients $\{c_k^L\}$ computed by the Galerkin approach:

$$(2.2) \quad \mathbf{G}^L \mathbf{c}^L = \mathbf{f}^L, \quad \mathbf{f}^L = (f_k^L)_{1 \leq k \leq K}, \quad f_k^L = \left\langle \mathbf{U}^L(z), \mathbf{U}^L(z_k) \right\rangle,$$

where \mathbf{G}^L is the Gramian matrix of $\mathcal{U}^L(\gamma_K)$,

$$(2.3) \quad (\mathbf{G}^L)_{ij} = \left\langle \mathbf{u}^L(z_i), \mathbf{u}^L(z_j) \right\rangle^L, \quad 1 \leq i, j \leq K,$$

with $\langle \cdot, \cdot \rangle^L$ the inner product associated with $\mathcal{U}^L(\gamma_K)$.

- 6 Construct the bi-fidelity approximation by applying the sample approximation rule as in the low-fidelity model:

$$(2.4) \quad \mathbf{U}^B(z) = \sum_{k=1}^K c_k^L(z) \mathbf{U}^H(z_k).$$

uniform error bound in H^1 norm for time-splitting Fourier pseudospectral methods for the long-time dynamics of the Schrödinger equation with small potential. On the other hand, asymptotic methods include the WKB methods [9] and various wave packets based methods [16, 30, 13, 21].

Define the spatial mesh size $h = \Delta x > 0$ with $h = (b - a)/M$ for M an even positive integer and choose the time step $\tau = \Delta t > 0$. Then let the grid points and the time step be

$$x_j := a + jh, \quad t_n := n\tau, \quad j = 0, 1, \dots, M, \quad n = 0, 1, 2, \dots$$

For any given z , let $\Psi_j^{\varepsilon, n}$ be the approximation of $\psi^\varepsilon(x_j, t_n, z)$. From time $t = t_n$ to time $t = t_{n+1}$, the Schrödinger equation (1.1) can be decomposed into the following two subproblems via the Strang splitting:

$$(2.7) \quad i\varepsilon \partial_t \psi + \frac{\varepsilon^2}{2} \partial_{xx} \psi = 0,$$

$$(2.8) \quad i\varepsilon \partial_t \psi - V(x, z) \psi = 0.$$

Equation (2.7) will be discretized in space by the spectral method and integrated in time exactly. Equation (2.8) will then be solved exactly. The detailed TSFP method

Algorithm 2.2 Tri-fidelity approximation for a high-fidelity solution at given z .

Offline:

1 Select a sample set $\Gamma_N = \{z_1, z_2, \dots, z_N\} \subset I_z$.

2 Low-fidelity simulations. Conduct simulations of the low-fidelity model $\mathbf{U}^L(z_j)$ for each $z_j \in \Gamma_N$ to obtain $\mathbf{U}^L(\Gamma_N)$ and the solution space $\mathcal{U}^L(\Gamma_N)$.

3 Points selection. Select K “important” points from Γ_N . Denote $\gamma_K = \{z_{i_1}, \dots, z_{i_K}\} \subset \Gamma_N$.

4 Medium- and high-fidelity simulations. Run both the medium-fidelity model and the high-fidelity simulation at each point in the selected sample set γ_K to obtain $\mathbf{U}^M(\gamma_K)$ and $\mathbf{U}^H(\gamma_K)$ and the corresponding medium-fidelity approximation space $\mathcal{U}^M(\gamma_K)$ and high-fidelity approximation space $\mathcal{U}^H(\gamma_K)$.

Online:

5 Best approximation in medium-fidelity solution space. For any given $z \in I_z$, compute the medium-fidelity solution $\mathbf{U}^M(z)$, and the corresponding medium-fidelity coefficients by projection:

$$(2.5) \quad \mathbf{U}^M(z) = \sum_{k=1}^K c_k^M(z) \mathbf{U}^M(z_{i_k}),$$

where the expansion coefficients $\mathbf{c}^M = (c_1^M, \dots, c_K^M)^T$ are computed by

$$\mathbf{G}^M \mathbf{c}^M = \mathbf{g}^M, \quad \mathbf{g}^M = (g_k^M)_{1 \leq k \leq K}, \quad g_k^M = \langle \mathbf{U}^M(z), \mathbf{U}^M(z_{i_k}) \rangle,$$

where \mathbf{G}^M is the Gramian matrix for $\mathcal{U}^M(\gamma_K)$,

$$(\mathbf{G}^M)_{lk} = \langle \mathbf{U}^M(z_{i_\ell}), \mathbf{U}^M(z_{i_k}) \rangle^M, \quad 1 \leq \ell, k \leq K,$$

with $\langle \cdot, \cdot \rangle^M$ the inner product associated with $\mathcal{U}^M(\gamma_K)$.

6 Tri-fidelity approximation. Construct the tri-fidelity approximation by applying the construction (2.5) to the high-fidelity solution ensemble $u^H(\gamma_K)$ to obtain

$$(2.6) \quad \mathbf{U}^T(z) = \sum_{k=1}^K c_k^M(z) \mathbf{U}^H(z_{i_k}).$$

for discretizing the Schrödinger equation (1.1) can be given for $n \geq 0$ as [4]

$$(2.9) \quad \begin{aligned} \Psi_j^{(*)} &= \sum_{l \in \mathcal{T}_N} e^{-i \frac{\varepsilon \tau \mu_l^2}{4}} (\widetilde{\Psi}^n)_l e^{i \mu_l (x_j - a)}, \\ \Psi_j^{(**)} &= e^{-i \frac{\tau}{\varepsilon} V(x_j, z)} \Psi_j^{(*)}, \quad j = 0, 1, 2, \dots, N, \\ \Psi_j^{n+1} &= \sum_{l \in \mathcal{T}_N} e^{-i \frac{\varepsilon \tau \mu_l^2}{4}} (\widetilde{\Psi}^{(**)})_l e^{i \mu_l (x_j - a)}, \end{aligned}$$

where

$$\widetilde{\Psi}_l^n = \frac{1}{N} \sum_{j=0}^{N-1} \Psi_j^n e^{-i \mu_l (x_j - a)}, \quad \mu_l = \frac{2\pi l}{b-a}, \quad l = -\frac{N}{2}, \dots, \frac{N}{2} - 1,$$

with $\Psi_j^0 = \Psi_0(x_j)$ for $j = 0, 1, 2, \dots, N$. Let $I_N u$ be the trigonometric interpolation

of a function u [26],

$$I_N u = \sum_{l=-N/2}^{N/2-1} \tilde{u}_l e^{i\mu_l(x-a)}, \quad \tilde{u}_l = \frac{1}{N} \sum_{j=0}^{N-1} u(x_j) e^{-i\mu_l(x_j-a)}, \quad l = -\frac{N}{2}, \dots, \frac{N}{2} - 1.$$

As a remark, we only focus on the case with one-dimensional spacial variable ($d = 1$). Generalization to $d > 1$ is straightforward for tensor product grids and the results remain valid without modifications.

2.2. Low-fidelity solvers. It is known that the low-fidelity models are not unique, in this section we will present several of our choices for the low-fidelity models. For convenience, we review the following low-fidelity solvers for the corresponding deterministic problems.

2.2.1. Frozen Gaussian Approximation (FGA) method. First we mention the motivation for adopting the FGA method.

The Eulerian-based methods suffer from the ‘‘curse of dimensionality’’, thus making them highly computationally expensive [14, 17]. For example, in the time splitting spectral method, the degree of freedom to approximate the wave function on a d -dimensional mesh is $O(\varepsilon^{-d})$. The so-called FGA type method [19], on the other hand, is one of the favourable schemes especially for high dimensional spatial problem. In [19], the authors conducted the error estimate for the FGA approximation with surface hopping to the matrix Schrödinger equation, which is an approximation to the Schrödinger equation

$$(2.10) \quad i\varepsilon \partial_t \psi = -\frac{\varepsilon^2}{2} \partial_{xx} \psi + V(x) \psi$$

with $\mathcal{O}(\varepsilon)$ error [27]. Denote by $z_0 = (q_0, p_0)$ the phase space variables. Assume that $A(0, z_0)$ is an integrable function in \mathbb{R}^{2d} , i.e., $\int_{\mathbb{R}^{2d}} |A(0, z_0)| dz_0 < \infty$. The usual FGA on a single surface [19] is given by

$$\begin{aligned} \psi_{\text{FGA}}(t, x) &= \frac{1}{(2\pi\varepsilon)^{3d/2}} \int_{\mathbb{R}^{2d}} A(t, z_0) \exp\left(\frac{i}{\varepsilon} \Theta(t, x, z_0)\right) dz_0 \\ &= \frac{1}{(2\pi\varepsilon)^{3d/2}} \int_{\mathbb{R}^{2d}} |A(0, z_0)| \frac{A(t, z_0)}{|A(0, z_0)|} \exp\left(\frac{i}{\varepsilon} \Theta(t, x, z_0)\right) dz_0, \end{aligned}$$

and the initial condition

$$\psi_0(x) = \frac{1}{(2\pi\varepsilon)^{3d/2}} \int_{\mathbb{R}^{2d}} A(0, z_0) \exp\left(\frac{i}{\varepsilon} \Theta(0, x, z_0)\right) dz_0,$$

where

$$\begin{aligned} \Theta(t, x, q, p) &= S(t, q, p) + P(t, q, p) \cdot (x - Q(t, q, p)) + \frac{i}{2} |x - Q(t, q, p)|^2, \\ A(t, q, p) &= a(t, q, p) \int_{\mathbb{R}^d} \psi_0(y) e^{\frac{i}{\varepsilon} (-p \cdot (y-q) + \frac{i}{2} |y-q|^2)} dy. \end{aligned}$$

Here, Gaussian profile Q and momentum function P are governed by the Hamiltonian flow associated to the classical Hamiltonian $h(q, p) = \frac{1}{2}|p|^2 + V(q)$. Action function S is associated to the Hamiltonian flow and the amplitude a is governed by corresponding evolution equations.

Define $T_{n:1} = (t_n, t_{n-1}, \dots, t_1)$ a partition of the time interval $[0, t]$ satisfying $0 \leq t_1 \leq t_2 \leq \dots \leq t_n \leq t$, with $t_0 = 0$. When $t \in [t_k, t_{k+1})$ for k being an integer, the evolution equations are given accordingly as

$$(2.11) \quad \begin{aligned} \frac{d}{dt} Q^{(k)} &= P^{(k)}, \\ \frac{d}{dt} P^{(k)} &= -\nabla V(Q^{(k)}), \\ \frac{d}{dt} S^{(k)} &= \frac{1}{2}(P^{(k)})^2 - V(Q^{(k)}), \\ \frac{d}{dt} A^{(k)} &= \frac{1}{2} A^{(k)} \operatorname{tr} \left((Z^{(k)})^{-1} \left(\partial_z P^{(k)} - i \partial_z Q^{(k)} \nabla_Q^2 V(Q^{(k)}) \right) \right). \end{aligned}$$

See Section 4 in [19] for the asymptotic derivation of these equations.

Define a probability measure \mathbb{P}_0 on \mathbb{R}^{2d} such that

$$(2.12) \quad \mathbb{P}_0(\Omega) = \mathcal{Z}^{-1} \frac{1}{(2\pi\varepsilon)^{3d/2}} \int_{\Omega} |A(0, z_0)| dz_0$$

for any $\Omega \subset \mathbb{R}^{2d}$, where $\mathcal{Z} = \frac{1}{(2\pi\varepsilon)^{3d/2}} \int_{\mathbb{R}^{2d}} |A(0, z_0)| dz_0$ is a normalization factor so that \mathbb{P}_0 is a probability measure. Then the FGA can be written as

$$(2.13) \quad \begin{aligned} \psi_{\text{FGA}}(t, x) &= \mathcal{Z} \int \frac{A(t, z_0)}{|A(0, z_0)|} \exp\left(\frac{i}{\varepsilon} \Theta(t, x, z_0)\right) \mathbb{P}_0(dz_0) \\ &= \mathcal{Z} \mathbb{E}_{z_0} \left[\frac{A(t, z_0)}{|A(0, z_0)|} \exp\left(\frac{i}{\varepsilon} \Theta(t, x, z_0)\right) \right], \end{aligned}$$

where the expectation is taken with respect to \mathbb{P}_0 . Thus, we may use a Monte Carlo sampling for $\psi_{\text{FGA}}(t, x)$ as

$$(2.14) \quad \psi_{\text{FGA}}(t, x) \approx \frac{\mathcal{Z}}{M} \sum_{i=1}^M \frac{A(t, z_0^{(i)})}{|A(0, z_0^{(i)})|} \exp\left(\frac{i}{\varepsilon} \Theta(t, x, z_0^{(i)})\right),$$

where $\{z_0^{(i)}\}_{i=1, \dots, M} \subset \mathbb{R}^{2d}$ are i.i.d. samples from the probability measure \mathbb{P}_0 .

2.2.2. The semiclassical limit and Liouville equation. When the Wigner transformation is applied to the Schrödinger equation, its semi-classical limit reveals a kinetic equation in phase space, which is known as the classical Liouville or Vlasov equation. In the semi-classical regime where the scaled Planck constant ε is small, the Liouville equation is a good approximation for the Schrödinger equation, thus one can choose it as a candidate of our low-fidelity models. The physical quantities of interests are position and current densities. When the ε is presumed small, the densities computed from the Schrödinger equation is an $O(\varepsilon)$ approximation to that obtained by the Vlasov equation using moments of the distribution function. Below we briefly review the Wigner transformation [2, 5, 11, 15].

Now let $\psi^\varepsilon(t)$ be the solution of (2.10) and denote $w^\varepsilon(t) := w^\varepsilon(\psi^\varepsilon(t), \psi^\varepsilon(t))$. Then w^ε satisfies the Wigner equation

$$(2.15) \quad \begin{aligned} w_t^\varepsilon + p \cdot \nabla_x w^\varepsilon + \Xi^\varepsilon[V]w^\varepsilon &= 0, \quad (x, p) \in \mathbb{R}_x^d \times \mathbb{R}_p^d, \quad t \in \mathbb{R}, \\ w^\varepsilon(t=0) &= w^\varepsilon(\psi_0^\varepsilon, \psi_0^\varepsilon), \end{aligned}$$

where $\Xi^\varepsilon[V]$ is the pseudo-differential operator,

$$\Xi^\varepsilon[V]w^\varepsilon(t, x, p) := \frac{i}{(2\pi)^d} \int_{\mathbb{R}_\alpha^d} \frac{V(x + \frac{\varepsilon}{2}\alpha) - V(x - \frac{\varepsilon}{2}\alpha)}{\varepsilon} \hat{w}^\varepsilon(t, x, \alpha) e^{i\alpha \cdot p} d\alpha,$$

where \hat{w}^ε stands for the Fourier transform $\mathcal{F}_{p \rightarrow \alpha} w^\varepsilon(t, x, \cdot) := \int_{\mathbb{R}_p^d} w^\varepsilon(t, x, p) e^{-i\alpha \cdot p} dp$. Taking ε to 0 and dropping the superscript 0 in w^0 give the following Vlasov (Liouville) equation

$$\begin{aligned} w_t + p \cdot \nabla_x w - \nabla_x V(x) \cdot \nabla_p w &= 0, \quad (x, p) \in \mathbb{R}_x^d \times \mathbb{R}_p^d, \quad t \in \mathbb{R}, \\ w(t=0) &= w_I := \lim_{\varepsilon \rightarrow 0} w^\varepsilon(\psi_0^\varepsilon, \psi_0^\varepsilon). \end{aligned}$$

For the semiclassical WKB initial data $\psi(x, 0) = A_0(x) e^{iS_0(x)/\varepsilon}$, w satisfies the following Liouville equation:

$$(2.16) \quad \begin{aligned} \partial_t w + p \cdot \nabla_x w - \nabla_x V \cdot \nabla_p w &= 0, \\ w(0, x, p) &= \rho_0(x) \delta(p - \nabla_x S_0). \end{aligned}$$

The level set (LS) method proposed in [12] solves the Liouville equation (2.16) by decomposing w into f and $\phi_i (i = 1, \dots, d)$, namely

$$w(t, x, p) := f(t, x, p) \prod_{i=1}^d \delta(\phi_i(t, x, p)),$$

each of which satisfies a Liouville equation with following initial conditions:

$$(2.17) \quad \begin{aligned} \partial_t f + p \cdot \nabla_x f - \nabla_x V(x) \cdot \nabla_p f &= 0, \\ f(0, x, p) &= \rho_0(x); \\ \partial_t \phi_i + p \cdot \nabla_x \phi_i - \nabla_x V(x) \cdot \nabla_p \phi_i &= 0, \\ \phi_i(0, x, p) &= p - \nabla_x S_0, \end{aligned}$$

Then the physical observables of the Liouville equation (2.16) are thus given by:

$$\rho(t, x) = \int f(t, x, p) \prod_{i=1}^d \delta(\phi_i) dp, \quad J(t, x) = \int p f(t, x, p) \prod_{i=1}^d \delta(\phi_i) dp.$$

3. Error estimates. In this section, we will establish an error estimate of a bi-fidelity method for the semiclassical Schrödinger equation with random parameters.

Let the high-fidelity solution be the macroscopic moments of density and momentum that are obtained from the solution Ψ to the Schrödinger equation (1.1) solved via TSFP method. Let D be the discrete approximation of the operation *grad*. Then define the high-fidelity solution \mathbf{U}^H of the Schrödinger equation (1.1) by the solution Ψ^H , i.e.,

$$\mathbf{U}^H = |\Psi^H|^2 := \rho^H.$$

Let the low-fidelity solution be the macroscopic moments obtained from the solution Ψ to the Schrödinger equation (1.1) solved via FGA method. Then define the low-fidelity solution \mathbf{U}^L of the Schrödinger equation (1.1) by the solution Ψ^L , i.e.,

$$\mathbf{U}^L = |\Psi^L|^2 := \rho^L.$$

Let the bi-fidelity solution \mathbf{U}^B (2.4) solved from the bi-fidelity approximation Algorithm 1. In order to obtain the error estimate of $\mathbf{U}^H - \mathbf{U}^B$ in general, we use the following way to split the total error, by inserting the information of u^L :

$$\begin{aligned}
(3.1) \quad & \mathbf{U}^H(z) - \mathbf{U}^B(z) \\
&= \mathbf{U}^H(z) - \sum_{k=1}^K c_k(z) \mathbf{U}^H(z_k) \\
&= \mathbf{U}^H(z) - \mathbf{U}^L(z) + \left(\mathbf{U}^L(z) - \sum_{k=1}^K c_k(z) \mathbf{U}^L(z_k) \right) + \sum_{k=1}^K c_k(z) \left(\mathbf{U}^L(z_k) - \mathbf{U}^H(z_k) \right),
\end{aligned}$$

where the second term is nothing but the projection error of the greedy algorithm, and it remains to estimate $\mathbf{U}^H(z) - \mathbf{U}^L(z)$ in proper norms.

3.1. Notations and prerequisites. We first define the space and norms that will be used. The Hilbert space of the random variable is given by

$$H(\mathbb{R}^d; \pi dz) = \left\{ f \mid I_z \rightarrow \mathbb{R}, \int_{I_z} f^2(z) \pi(z) dz < \infty \right\},$$

and equipped with the inner product $\langle f, g \rangle_\pi = \int_{I_z} f g \pi(z) dz$. We introduce the standard multivariate notation. Denote the countable set of "finitely supported" sequences of non-negative integers by

$$\mathcal{F} := \{ \nu = (\nu_1, \nu_2, \dots) : \nu_j \in \mathbb{N}, \text{ and } \nu_j \neq 0 \text{ for only a finite number of } j \}$$

with $|\nu| := \sum_{j \geq 1} \nu_j$. For $\nu \in \mathcal{F}$ supported in $\{1, \dots, J\}$, the partial derivative in z is defined by $\partial_z^\nu = \frac{\partial^{|\nu|}}{\partial^{\nu_1} z_1 \dots \partial^{\nu_J} z_J}$. The z -derivative of order ν of a function f is denoted by $f^\nu = \partial_z^\nu f$.

Now we introduce some prerequisites that will be used later for the FGA and TSFP numerical schemes. In the following two lemmas, for simplicity of notations, we consider the deterministic problem setting. The error estimate for FGA is reviewed in Lemma 3.2 under Assumption 3.1; the error estimate for TSFP is obtained based on [4] and summarized in Lemma 3.4 under Assumption 3.3. We give the proof of Lemma 3.4 in Appendix A.

Assumption 3.1. $V(q) \in C^\infty(\mathbb{R}^d)$ satisfies $\sup_{q \in \mathbb{R}^d} |\partial_\alpha V(q)| \leq C_V$, for $|\alpha| = 2$.

Assume that there exists a compact set $K \subset \mathbb{R}^{2d}$ such that the initial approximation error, given by

$$(3.2) \quad \epsilon_{\text{in}} = \left\| \frac{1}{(2\pi\varepsilon)^{3d/2}} \int_K A^{(0)}(0, z) e^{\frac{i}{\varepsilon} \Phi^{(0)}(0, x, z)} dz - u_0(0, x) \right\|_{L^2(\mathbb{R}^d)} > 0,$$

is sufficiently small for the accuracy requirement.

LEMMA 3.2. [19] *Let $\Psi_{FGA}(t, x)$ be the approximation given by the FGA (with phase space integral restricted to the set K) for the Schrödinger equation (2.10), whose exact solution is denoted by $\psi(t, x)$. Under Assumption 3.1, for any given final time t , there exists a constant C , such that for any $\varepsilon > 0$ sufficiently small, we have*

$$\|\Psi_{FGA}(t, x) - \psi(t, x)\|_{L^2(\mathbb{R}^d)} \leq C\varepsilon + \epsilon_{\text{in}},$$

where ϵ_{in} is the initial approximation error defined in (3.2).

Assumption 3.3. Assume that the exact solution $\psi(t, x)$ of the Schrödinger equation (2.10) and the potential satisfy

$$\|\psi(t, x)\|_{L^\infty([0, T_\varepsilon]; H_{\text{per}}^m)} \leq \frac{C}{\varepsilon^m}, \quad V(x) \in H_{\text{per}}^{m^*}, \quad m^* = \max\{m, 4\},$$

where m describes the regularity of the exact solution. Here, $H_{\text{per}}^m(\Omega) = \{\psi \in H^m(\Omega) \mid \partial_x^k \psi(a) = \partial_x^k \psi(b), k = 0, 1, \dots, m-1\}$, with the equivalent H^m -norm on $H_{\text{per}}^m(\Omega)$ given as $\|\psi\|_{H^m} = (\sum_{l \in \mathbb{Z}} (1 + \mu_l^2)^m |\widehat{\psi}_l|^2)^{1/2}$.

LEMMA 3.4. *Let ψ^n be the numerical approximation obtained from the TSFP (2.9). Under Assumption 3.3, for any $0 < \varepsilon \leq 1$, $t_n \in [0, T]$, we have*

$$(3.3) \quad \|\psi(t_n, x) - I_N \psi^n\|_{L^2} \leq C_0 G_m \frac{T}{\varepsilon} \left(h^m + \frac{\tau^2}{\varepsilon^3} \right), \quad m \geq 2,$$

where C_0 and C_1 are positive constants independent of $\varepsilon, h, \tau, n, m$; G_m is a positive constant independent of ε, h, τ, n and only depends on $\|\psi\|_{L^\infty([0, T]; L^2)}$ and $\|V\|_{L^2}$.

3.2. Main result. Now we introduce the main result on the bi-fidelity method in Theorem 3.6 under Assumption 3.1, Assumption 3.3 and Assumption 3.5. Here TSFP is used as the high-fidelity solver and FGA is chosen as the low-fidelity model.

Assumption 3.5. Assume each component of the random variable $z := (z_j)_{j \geq 1}$ has a compact support. Let $(\psi_j)_{j \geq 1}$ be an affine representer of the random initial data ψ_{in} , which by definition means that [7]

$$(3.4) \quad \psi_{\text{in}}(z) = \tilde{\psi}_0 + \sum_{j \geq 1} z_j \phi_j,$$

where $\tilde{\psi}_0 = \tilde{\psi}_0(x)$ is independent of z , and the sequence $\{\|\phi_j\|_{L^\infty(\Omega)}\}_{j \geq 1} \in \ell^p$ for $0 < p < 1$, with Ω representing the physical space.

The reason we need to assume a compact support of random variable z and (3.4) is because of [7], which is used for the projection error estimate for greedy algorithm. We now show the main result:

THEOREM 3.6. *Let Assumption 3.1, Assumption 3.3, Assumption 3.5 hold, and $\mathbf{U}^H, \mathbf{U}^B$ represent the high- and bi-fidelity approximation for the position density solved from the Schrödinger equation (1.1). With K high-fidelity simulation runs, the error estimate of the bi-fidelity method is given by*

$$\left\| \mathbf{U}^H(z) - \mathbf{U}^B(z) \right\|_{L_x^2 L_z^2} \leq \frac{C_1}{\varepsilon} \frac{1}{(K/2 + 1)^{q/2}} + C_2 \sqrt{\frac{K}{\lambda_0}} \left(\varepsilon + \frac{T}{\varepsilon} \left(h^m + \frac{\tau^2}{\varepsilon^3} \right) + \varepsilon_{\text{in}} \right),$$

where C_1, C_2 are constants independent of ε ; m depends on the regularity of the exact solution ψ as shown in Assumption 3.3; λ_0 is the minimum eigenvalue of the Gramian matrix defined in (2.3); q is independent of dimensionality of z ; h and τ are spatial and temporal sizes.

Now we show the proof for Theorem 3.6.

Proof. Taking $\|\cdot\|_{L_x^2 L_z^2}$ norm on both sides of the equality (3.1) for the moments,

one has

$$\begin{aligned}
 (3.5) \quad & \left\| \mathbf{U}^H(z) - \mathbf{U}^B(z) \right\|_{L_x^2 L_z^2} = \left\| \mathbf{U}^H(z) - \sum_{k=1}^K c_k^L(z) \mathbf{U}^H(z_k) \right\|_{L_x^2 L_z^2} \\
 & \leq \underbrace{\left\| \mathbf{U}^H(z) - \mathbf{U}^L(z) \right\|_{L_x^2 L_z^2}}_{\text{Term } A_1} + \underbrace{\left\| \mathbf{U}^L(z) - \sum_{k=1}^K c_k^L(z) \mathbf{U}^L(z_k) \right\|_{L_x^2 L_z^2}}_{\text{Term } A_2} \\
 & \quad + \underbrace{\left\| \sum_{k=1}^K c_k^L(z) \left(\mathbf{U}^L(z_k) - \mathbf{U}^H(z_k) \right) \right\|_{L_x^2 L_z^2}}_{\text{Term } A_3}.
 \end{aligned}$$

Let $\mathbf{U}^{H,L} := \boldsymbol{\rho}^{H,L}$ be the high- or low-fidelity approximation for the position density, and assume $\mathbf{u} = \boldsymbol{\rho}$ be the exact solution obtained from ψ that solves the Schrödinger equation. The first term A_1 is estimated by $\left\| \mathbf{U}^H - \mathbf{u} \right\|_{L_x^2 L_z^2}$ and $\left\| \mathbf{U}^L - \mathbf{u} \right\|_{L_x^2 L_z^2}$. The second term A_2 is actually the projection error of the greedy algorithm when searching the most important points γ_K from the low-fidelity solution manifold. To estimate the third term A_3 , a bound for the vector $\|\mathbf{c}\|$ with $\|\cdot\|$ the matrix induced ℓ_2 norm is obtained and then the Cauchy-Schwarz inequality is applied.

Now that

$$\left\| \mathbf{U}^H(z) - \mathbf{U}^L(z) \right\|_{L_x^2 L_z^2} \leq \left\| \mathbf{U}^H - \mathbf{u} \right\|_{L_x^2 L_z^2} + \left\| \mathbf{u} - \mathbf{U}^L \right\|_{L_x^2 L_z^2}.$$

Since $\mathbf{U} = \boldsymbol{\rho} = |\psi|^2$, then $\|\mathbf{U}\|_{L_x^2 L_z^2} = \|\boldsymbol{\rho}\|_{L_x^2 L_z^2} \leq \|\psi\|_{L_x^2 L_z^2}^2$. Let $\Psi_{TSFP}(t, x, z)$ be the numerical approximation obtained from the TSFP. Let $\Psi_{FGA}(t, x, z)$ be the approximation solved by the FGA and $\psi(t, x, z)$ be the exact solution. Then, the following estimate holds from Lemma 3.4 and Lemma 3.2:

$$\begin{aligned}
 (3.6) \quad & \left\| \mathbf{U}_{FGA}^L - \mathbf{U}_{TSFP}^H \right\|_{L_x^2 L_z^2} \leq \left\| \mathbf{U}_{FGA}^L - \mathbf{u} \right\|_{L_x^2 L_z^2} + \left\| \mathbf{u} - \mathbf{U}_{TSFP}^H \right\|_{L_x^2 L_z^2} \\
 & \lesssim \left\| \Psi_{FGA}^L - \psi \right\|_{L_x^2 L_z^2} + \left\| \psi - \Psi_{TSFP}^H \right\|_{L_x^2 L_z^2} \\
 & \leq C \left(\varepsilon + \frac{T}{\varepsilon} \left(h^m + \frac{\tau^2}{\varepsilon^3} \right) \right) + \epsilon_{in}.
 \end{aligned}$$

The second term A_2 in (3.5) is evaluated by the Kolmogorov K -width of a functional manifold, which characterizes the optimal distance for approximation from a general K -dimensional subspace [10, 18]. Denote by $d_K(\mathbf{U}^L(I_z))$ the Kolmogorov K -width of the functional manifold $\mathbf{U}^L(I_z)$, defined by

$$d_K(\mathbf{U}^L(I_z)) = \inf_{\dim(V_K)=K} \sup_{v \in \mathbf{U}^L(I_z)} d^L(v, V_K).$$

Denote the space $\mathcal{H} = L_x^2$. Specifically, one has

$$\begin{aligned}
 (3.7) \quad & d_K(\mathbf{U}^L(I_z))_{\mathcal{H}} \leq \sup_{v \in \mathbf{U}^L(I_z)} \min_{w \in V_K} \|v - w\|_{\mathcal{H}} = \sup_{z \in I_z} \min_{w \in V_K} \left\| \mathbf{U}^L(z) - w \right\|_{\mathcal{H}} \\
 & \leq \left\| \mathbf{U}^L - \sum_{\nu \in \Lambda_K} w_\nu P_\nu \right\|_{L^\infty(I_z, \mathcal{H})} \leq \frac{C}{\varepsilon} \frac{1}{(K+1)^q}, \quad q = \frac{1}{p} - 1,
 \end{aligned}$$

which holds for all z . Then

$$(3.8) \quad \left\| \mathbf{U}^L - \sum_{\nu \in \Lambda_K} w_\nu P_\nu \right\|_{L_x^2 \mathcal{H}} \leq \frac{C}{\varepsilon} \frac{1}{(K+1)^q}, \quad q = \frac{1}{p} - 1,$$

based on the analysis of the bound for $\partial_z \rho$ in Appendix C. Here p is a constant associated with the affine representer $(\psi_j)_{j \geq 1}$ in the random initial data specified by Eq. (3.4). In addition, $\sum_{\nu \in \Lambda_K} w_\nu P_\nu$ is the truncated Legendre expansion with $(P_k)_{k \geq 0}$ the sequence of renormalized Legendre polynomials on $[-1, 1]$, and Λ_K is the set of indices corresponding to the K largest $\|w_\nu\|_{\mathcal{H}}$. Plugging $K/2$ into Eq. (3.8),

$$(3.9) \quad \text{Term } A_2 \leq \frac{C_1}{\varepsilon} \frac{1}{(K/2 + 1)^{q/2}}.$$

For the third term A_3 , one has

$$(3.10) \quad \left(\sum_{k=1}^K \|c_k(z)\|_{L_x^2}^2 \right)^{1/2} \lesssim \frac{1}{\sqrt{\lambda_0}} \left\| \mathbf{U}^L(z) \right\|_{L_x^2 L_z^2},$$

where λ_0 is the smallest eigenvalue of the Gramian matrix \mathbf{G}_L defined in (2.3). Details for (3.10) are given in Appendix B. By the Cauchy-Schwarz inequality, combining (3.6) and (3.10), one gets

$$(3.11) \quad \begin{aligned} \text{Term } A_3 &\leq \left(\sum_{k=1}^K \|c_k(z)\|^2 \right)^{1/2} \left(\sum_{k=1}^K \left\| \mathbf{U}^H(z_k) - \mathbf{U}^L(z_k) \right\|_{L_x^2 L_z^2}^2 \right)^{1/2} \\ &\lesssim \left(\sum_{k=1}^K \|c_k(z)\|_{L_x^2}^2 \right)^{1/2} \left(\sum_{k=1}^K \left\| \mathbf{U}^H(z_k) - \mathbf{U}^L(z_k) \right\|_{L_x^2}^2 \right)^{1/2} \\ &\leq \sqrt{N} \left(\sum_{k=1}^K \|c_k(z)\|_{L_x^2}^2 \right)^{1/2} \left(\max_k \left\| \mathbf{U}^H(z_k) - \mathbf{U}^L(z_k) \right\|_{L_x^2} \right) \\ &\leq \frac{\sqrt{K}}{\sqrt{\lambda_0}} \left(C' \left(\varepsilon + \frac{T}{\varepsilon} \left(h^m + \frac{\tau^2}{\varepsilon^3} \right) \right) + \epsilon_{in} \right) \left\| \mathbf{U}^L(z) \right\|_{L_x^2 L_z^2} \\ &\leq C \sqrt{\frac{K}{\lambda_0}} \left(\varepsilon + \frac{T}{\varepsilon} \left(h^m + \frac{\tau^2}{\varepsilon^3} \right) + \epsilon_{in} \right). \end{aligned}$$

Finally, by adding up (3.6), (3.9) and (3.11), the proof is completed from (3.5).

Remark 3.7. Note that if we want to give an error estimate for the tri-fidelity

method, one has

$$\begin{aligned}
 (3.12) \quad & \left\| \mathbf{U}^H(z) - \mathbf{U}^T(z) \right\|_{L_x^2 L_z^2} = \left\| \mathbf{U}^H(z) - \sum_{k=1}^K c_k^M(z) \mathbf{U}^H(z_k) \right\|_{L_x^2 L_z^2} \\
 & \leq \underbrace{\left\| \mathbf{U}^H(z) - \mathbf{U}^M(z) \right\|_{L_x^2 L_z^2}}_{\text{Term } A_1} + \underbrace{\left\| \mathbf{U}^M(z) - \sum_{k=1}^K c_k^M(z) \mathbf{U}^M(z_k) \right\|_{L_x^2 L_z^2}}_{\text{Term } A_2} \\
 & + \underbrace{\left\| \sum_{k=1}^K c_k^M(z) \left(\mathbf{U}^M(z_k) - \mathbf{U}^H(z_k) \right) \right\|_{L_x^2 L_z^2}}_{\text{Term } A_3}.
 \end{aligned}$$

Compared to (3.5), we substitute \mathbf{U}^L by \mathbf{U}^M in (3.12). Thus if $\left\| \mathbf{U}^H(z) - \mathbf{U}^M(z) \right\|_{L_x^2 L_z^2} \leq \left\| \mathbf{U}^H(z) - \mathbf{U}^L(z) \right\|_{L_x^2 L_z^2}$, then $\left\| \mathbf{U}^H(z) - \mathbf{U}^T(z) \right\|_{L_x^2 L_z^2} \leq \left\| \mathbf{U}^H(z) - \mathbf{U}^B(z) \right\|_{L_x^2 L_z^2}$, which indicates that the tri-fidelity method is more accurate than the bi-fidelity method where the same low-fidelity solver is chosen for both bi- and tri-fidelity method. Moreover, the “K” important points $\{z_{i_1}, z_{i_2}, \dots, z_{i_K}\}$ in the tri-fidelity method are chosen based on the low-fidelity solver, which is computationally much cheaper than the medium-fidelity solver. Therefore it is necessary to develop multi-fidelity methods.

4. Numerical examples. To examine the performance and accuracy of our proposed methods, the numerical errors are defined below. We choose a fixed set of points $\{\hat{z}_i\}_{i=1}^N \subset I_z$ that is independent of the point sets Γ , and evaluate the following error between the bi-(or tri-) fidelity and high-fidelity solutions at a final time t :

$$(4.1) \quad \mathcal{E} \approx \frac{1}{N} \sum_{i=1}^N \left\{ \frac{1}{N_x} \sqrt{\sum_{j=1}^{N_x} |u^H(t, x_j, \hat{z}_i) - u^M(t, x_j, \hat{z}_i)|^2} \right\},$$

where u^M represents the bi-fidelity or tri-fidelity approximations, and $\|\cdot\|_{L^2(\mathcal{X})}$ is the L^2 norm in the physical domain \mathcal{X} . The error can be considered as an approximation to the average L^2 error in the whole space of $\mathcal{X} \times I_z$.

Since our goal is to numerically compute the Schrödinger equation with random inputs, thus the high-fidelity model is always chosen as the TSFP method for solving the Schrödinger equation described in Section 2.1. The low-fidelity solver will be considered as the FGA method discussed in Section 2.2.1 or the LS method stated in Section 2.2.2.

The corresponding CFL condition for the Liouville equation is

$$\Delta t \leq \frac{\Delta x}{2 \max_{(x,p) \in \Omega} (p, \nabla_x V)}.$$

If we employ the LS method in our bi (tri)-fidelity solvers, we will use the simple piecewise linear kernel

$$\delta_\eta^{(1)}(x) = \begin{cases} \frac{1}{\eta} \left(1 - \frac{|x|}{\eta}\right), & \left| \frac{x}{\eta} \right| \leq 1, \\ 0, & \left| \frac{x}{\eta} \right| > 1, \end{cases} \quad \delta_\eta^{(2)}(x) = \begin{cases} \frac{1}{2\eta} \left(1 + \cos \frac{\pi|x|}{\eta}\right), & \left| \frac{x}{\eta} \right| \leq 1, \\ 0, & \left| \frac{x}{\eta} \right| > 1, \end{cases}$$

which have the so-called “exact integration property”:

$$\sum_{j=-N}^N \delta_{\kappa_0 h}^{(k)}(x_j - x_0) h = 1, \quad \text{for any } -Nh < x_0 < Nh, \quad k = 1, 2.$$

In our numerical tests, we use the kernel $\delta_\eta^{(2)}(x)$ and approximate the gradients $\nabla_x \phi$, $\nabla_p \phi$ by the upwind scheme with a fifth order WENO approximation, For time discretization, the 3rd order TVD Runge-Kutta scheme [5] is adopted. For the FGA solver, the time evolution ODEs (2.11) is computed by the forth-order Runge-Kutta scheme [19].

Without loss of generality, the d -dimensional random variables \mathbf{z} are assumed to follow the uniform distribution on $[-1, 1]^d$. Let the size of training set Γ to be $M = 1000$, and we evaluate the errors of bi (tri)-fidelity approximation with respect to the number of high-fidelity runs by computing the norm defined in (4.1) over an independent set of $N = 1000$ Monte Carlo samples.

In our test problems, the initial condition in (1.1) is always chosen as the classical WKB form

$$u^\varepsilon(t = 0, x) = u_0^\varepsilon(x) = \sqrt{n_0(x)} e^{iS_0(x)/\varepsilon},$$

with real valued n_0 and S_0 independent of ε , regular enough, and with $n_0(x)$ decaying to zero sufficiently fast as $|x| \rightarrow \infty$. We choose an appropriate interval $[a, b]$ for the computations such that the periodic boundary conditions do not introduce a significant error relative to the whole space problem. A Neumann boundary condition is presumed in the p direction.

4.1. Test 1. The initial condition is taken as

$$n_0(x, \mathbf{z}) = \left(\exp \left(-50 \left(1 + 0.8 \sum_{k=1}^{d_1} \frac{z_k^p}{2k} \right) \left(x - 1 + 0.2 \sum_{k=1}^{d_1} \frac{z_k^q}{2k} \right)^2 \right) \right)^2,$$

$$S_0(x, \mathbf{z}) = -\frac{1}{5} \ln \left(\exp \left(5(x - 1 + 0.2 \sum_{k=1}^{d_1} \frac{z_k^r}{2k}) \right) + \exp \left(-5(x - 1 + 0.2 \sum_{k=1}^{d_1} \frac{z_k^s}{2k}) \right) \right).$$

This example was based on [5], with uncertainties added to the initial condition. We solve on the x -interval $[0, 2]$ with periodic boundary conditions. Let $V(x) = 10$ be a constant potential.

Here $\mathbf{z}^R = (z_1^R, \dots, z_{d_1}^R)$ with $R = \{p, q, r, s\}$ represents the random variables shown in the initial condition. We set $d_1 = 5$, then the total dimension d of the random space is 20 in our problem settings. In Example 1, we vary ε from $1/64$ to $1/256$ and compare two different low-fidelity solvers. We employ the FGA method or LS method as the low-fidelity solver in Case I and II, respectively. In both cases, the TSFP method is chosen as the high-fidelity solver. When $\varepsilon = 1/64$, we utilize the FGA method with spatial mesh size $\Delta x_{FGA} = 0.0312$ for the low-fidelity solver in Case I; and the LS method with $\Delta x_{LS} = 0.01, \Delta p = 0.1$ for the low-fidelity solver in Case II. The range of p in this example is $[-2, 2]$. In TSFP method, $\Delta x_{TSFP} = 0.001$ is chosen. When $\varepsilon = 1/256$, we let the low-fidelity solver 1 (FGA) with $\Delta x_{FGA} = 0.0078$, the low-fidelity solver 2 (LS) with $\Delta x_{LS} = 0.0026, \Delta p = 0.1$, and the high-fidelity model (TSFP) with $\Delta x_{TSFP} = 0.00026$. We take $\Delta t = 10^{-5}$ in all these methods, 500 number of particles when $\varepsilon = 1/64$ and 1300 number of particles when $\varepsilon = 1/256$ in the FGA solver.

First, we investigate the performance of the bi-fidelity approximation for two kinds of low-fidelity solvers. From Figure 1, fast convergence of the mean L^2 errors between the high- and bi-fidelity solutions with respect to the number of high-fidelity runs is observed. Here Err_1 in the figures below stands for the errors of ρ , and Err_2 stands for the errors of J . This is corresponding to the error estimate analysis in Section 3, where we denote the bi-fidelity solution by $\mathbf{u} = (\rho, J)^T$. With only 10 high-fidelity runs, the bi-fidelity approximation can reach an accuracy level of $\mathcal{O}(10^{-3})$ for a 20-dimensional problem in random space, which is quite satisfactory compared to other sparse grid type of methods. We can observe that the smaller ε is, the lower level the errors (Err_1, Err_2) achieve when they saturate. Here Err_1, Err_2 stand for the errors calculated by (4.1) for ρ and J respectively. For example, comparing the two orange lines in the left and right part of Figure 1, the Err_1 decreases when ε becomes smaller, since the discrepancy between the low-fidelity model chosen as the Liouville equation and the high-fidelity model known by the Schrödinger equation is reduced when ε becomes smaller.

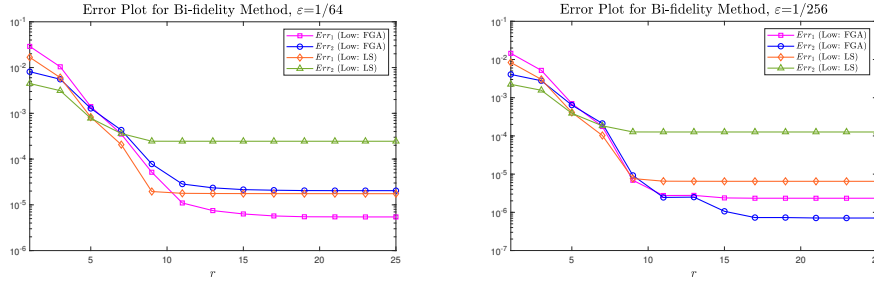


FIG. 1. Test 1: Case I and Case II. The mean L^2 error of the bi-fidelity approximation ρ, J with respect to the number of high-fidelity runs for different ε .

To illustrate the efficiency of the bi-fidelity method, we compare with the stochastic collocation (SC) method [29] here. Let $\{\mathbf{z}^{(m)}\}_{m=1}^{N_c} \subset I_{\mathbf{z}}$ be the set of collocation nodes, N_c the number of samples in the random space. For each individual sample $\mathbf{z}^{(m)}$, one applies the TSFP solver to the deterministic Schrödinger equation and obtains the solution ensemble $\mathbf{u}(t, x, \mathbf{z}^{(m)})$, then adopts the Legendre-Gauss quadrature rule to construct the approximation for the mean value $\bar{\mathbf{u}}_{N_c}(t, x) = \sum_{m=1}^{N_c} \mathbf{u}(t, x, (\mathbf{z}^{(m)})) w_j$, where w_j are the corresponding quadrature weights. We let the dimensionality of z to be $d_1 = 1$ and $N_{ref} = 256$ as a reference solution. We plot the error

$$Err_{j, N_c} = \|\bar{\mathbf{u}}_{j, N_c} - \bar{\mathbf{u}}_{j, N_{ref}}\|_{l^2}, \quad j = 1, 2,$$

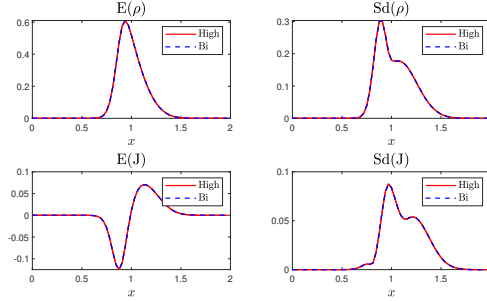
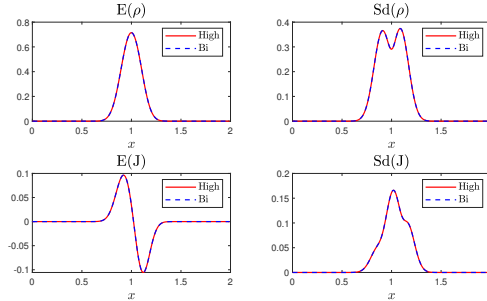
ranging from $N_c = 8$ to $N_c = 128$ as shown in Table 1. One can conclude that more than a hundred collocation points are needed to achieve 10^{-4} accuracy level for the SC method, while we just need to run the high-fidelity solver in the online stage of $\mathcal{O}(10)$ times, in order to achieve the same level of accuracy.

Figure 2 and Figure 3 show clearly that the mean and standard deviation of the bi-fidelity approximation for ρ and J agree well with the high-fidelity solutions by using only 20 high-fidelity runs for both two cases (FGA as low-fidelity for Case I and LS as low-fidelity for Case II). The result is a bit surprising yet reasonable, suggesting that although coarser mesh grid in the physical space is taken in both cases, the bi-fidelity approximation can still capture important variations of the high-fidelity model in the random space.

	N_c	8	16	32	64	128
$\varepsilon = 1/64$	Err_1	0.1583	0.0418	0.0106	0.0026	5.17e-04
	Err_2	0.0970	0.0257	0.0066	0.0016	3.19e-04
$\varepsilon = 1/256$	Err_1	0.3607	0.0951	0.0242	0.0058	0.0012
	Err_2	0.2455	0.0650	0.0166	0.0040	8.06e-04

TABLE 1

Tab. 1. Relative Error of the stochastic Collocation method for TSFP.

FIG. 2. Test 1: Case I. The mean and standard deviation of high- and bi-fidelity solutions ρ and J with $r = 25, \varepsilon = 1/256$ at $t = 0.5s$ with FGA and TSFP for the low- and high-fidelity solver.FIG. 3. Test 1: Case II. The mean and standard deviation of high- and bi-fidelity solutions ρ and J with $r = 25, \varepsilon = 1/64$ at $t = 0.01s$ with LS and TSFP for the low- and high-fidelity solver.

Regarding the tri-fidelity method, since the LS solver with finer meshes is more expensive than FGA, we choose FGA as the low-fidelity and LS as the medium-fidelity solver. The mean and standard deviation of the bi-fidelity solutions ρ and J are shown in Figures 4 and 5 with $\varepsilon = 1/64$ and $\varepsilon = 1/256$ respectively, by evaluating the medium- and high-fidelity method only 25 times at $t = 0.01$. Comparisons of the low-fidelity solution (FGA), medium-fidelity solution (LS), high-fidelity solution (TSFP) and the corresponding tri-fidelity approximations for an arbitrarily chosen sample point z are also shown in Figure 4 and 5. We can observe from the third row of Figure 4 and 5 that although the low- and medium-fidelity solutions are not accurate especially at positions where sharp transitions happen, yet the tri-fidelity approximation can still capture the solution well with random initial data.

Besides, we design another tri-fidelity method: based on the bi-fidelity method in Case I, keeping the low-fidelity (FGA) and high-fidelity (TSFP) solver unchanged,

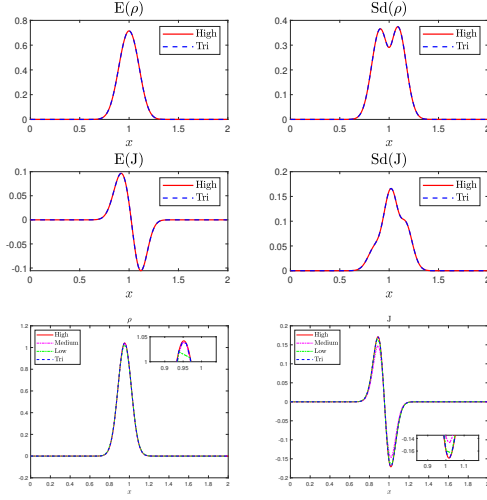


FIG. 4. *Test 1. The mean and standard deviation of high- and tri-fidelity solutions ρ and J with $r = 25, \varepsilon = 1/64$ at $t = 0.01$, and comparison of the low-fidelity (FGA), medium-fidelity (LS), high-fidelity (TSFP) solution and the corresponding tri-fidelity approximations for fixed z .*

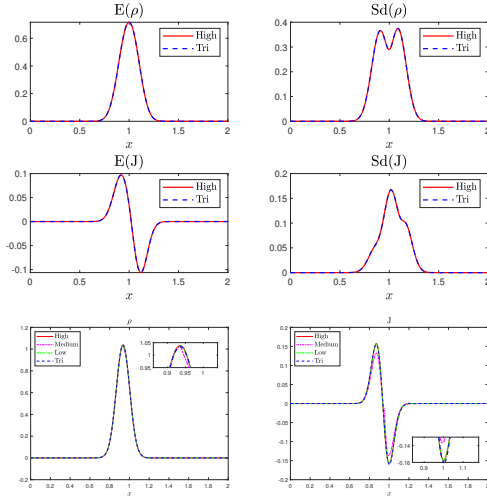


FIG. 5. *Test 1. The mean and standard deviation of high- and tri-fidelity solutions ρ and J with $r = 25, \varepsilon = 1/256$ at $t = 0.01$, and comparison of the low-fidelity (FGA), medium-fidelity (LS), high-fidelity (TSFP) solution and the corresponding tri-fidelity approximations for fixed z .*

and using the TSFP method with the coarser grid ($N_{TSFP}^H = 10N_{TSFP}^M$) as the medium-fidelity solver. We can see from Figure 6 that the mean L^2 error of the tri-fidelity solution decays much more quickly than that of the bi-fidelity method for $r > 10$. Figure 6 shows that the tri-fidelity method performs better than the bi-fidelity method in this example.

Below we make some remarks based on our experience of numerical simulations, between the medium- and low-fidelity solvers, we tend to choose the more expensive one as the medium-fidelity solver, which we only have to run K ($K \ll N$) times.

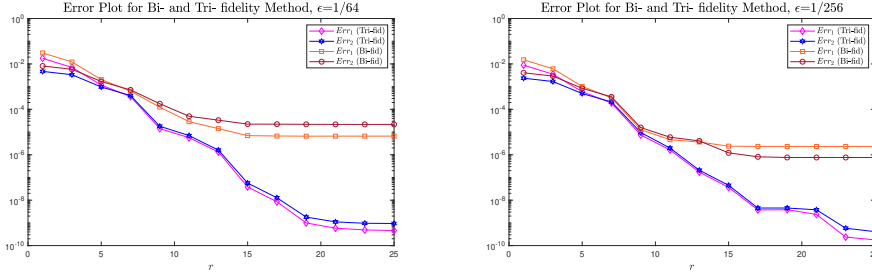


FIG. 6. *Test 1: Case I. The mean L^2 error of the bi-fidelity and tri-fidelity approximation ρ, J with respect to the number of high-fidelity runs for different ε .*

Since one needs to explore the low-fidelity solution space by repeatedly running the low-fidelity solvers N times (with N significantly large), the cheapest solver is always chosen as the low-fidelity model, regardless of its accuracy compared with medium-, not to say the high-fidelity solvers. Finally, it is noted that between the medium- and high-fidelity solvers, we always choose the more accurate one as the high-fidelity solver.

4.2. Test 2. The initial condition is assumed by

$$(4.2) \quad n_0(x, z) = \exp \left(- \left(1 + 0.6 \sum_{k=1}^{d_1} \frac{z_k^a}{2k} \right) \left(x + 1 - 0.4 \sum_{k=1}^{d_1} \frac{z_k^b}{2k} \right)^2 / \varepsilon \right),$$

$$S_0(x) = x + 1 - 0.4 \sum_{k=1}^{d_1} \frac{z_k^c}{2k}, \quad x \in \mathbb{R}.$$

This example was based on [5], where we add uncertainties to the initial condition. Let $V(x) = x^2/2$, which is a harmonic oscillator. In Test 2, the spatial domain is chosen to be $[-\pi, \pi]$, and periodic boundary condition is assumed. Here $\mathbf{z}^a = (z_1^a, \dots, z_{d_1}^a)$, $\mathbf{z}^b = (z_1^b, \dots, z_{d_1}^b)$ and $\mathbf{z}^c = (z_1^c, \dots, z_{d_1}^c)$ represent the random variables in initial condition of $n_0(x)$ and $S_0(x)$. Set $d_1 = 5$, thus this is a $d = 20$ dimensional problem in the random space.

We first choose FGA as the low-fidelity solver, TSFP as the high-fidelity solver and investigate the long-time behavior of the bi-fidelity solution. We consider the two different regimes with ε varying from $\varepsilon = 1/32$ to $\varepsilon = 1/128$ in this test. When we choose $\varepsilon = 1/32$, we take $N_{FGA} = 384$ and $N_{TSFP} = 10N_{FGA}$ grid points for FGA and TSFP method. When $\varepsilon = 1/128$, for spatial discretization, we take $N_{FGA} = 1536$ and $N_{TSFP} = 5N_{FGA}$ grid points for FGA and TSFP method. Let $\Delta t = \Delta x/20$ in both high- and low-fidelity models, with the final time $T = 6.0$. We choose 800 number of particles when $\varepsilon = 1/32$ and 1300 particles when $\varepsilon = 1/128$ for the FGA method.

Figure 7 shows the mean L^2 errors of ρ and J between the high- and bi-fidelity solutions with different ε . It is clear that the error decays fast with the number of high-fidelity runs. In addition, when ε decreases, the error between the high- and bi-fidelity solutions grows smaller.

In this test, the mean and standard deviation of the bi-fidelity solutions ρ and J are shown in Figure 8 with $\varepsilon = 1/32$ and Figure 10 with $\varepsilon = 1/128$ by adopting the high-fidelity solver only 25 times at both $t = 1$ and $t = 6$. We can see that all

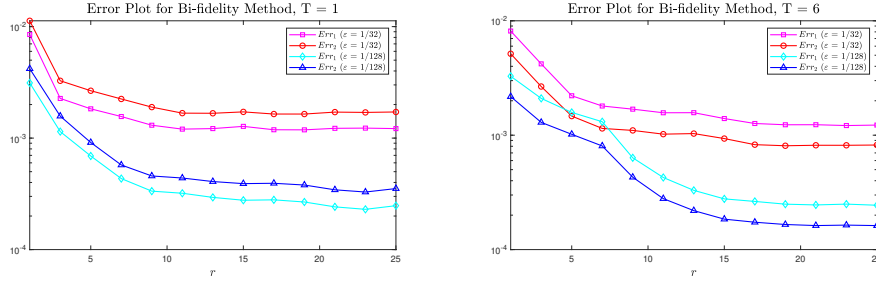


FIG. 7. Test 2. The mean L^2 errors of the bi-fidelity approximation ρ, J with respect to the number of high-fidelity runs for different ε . Here, Err_1, Err_2 stand for the errors of ρ and J .

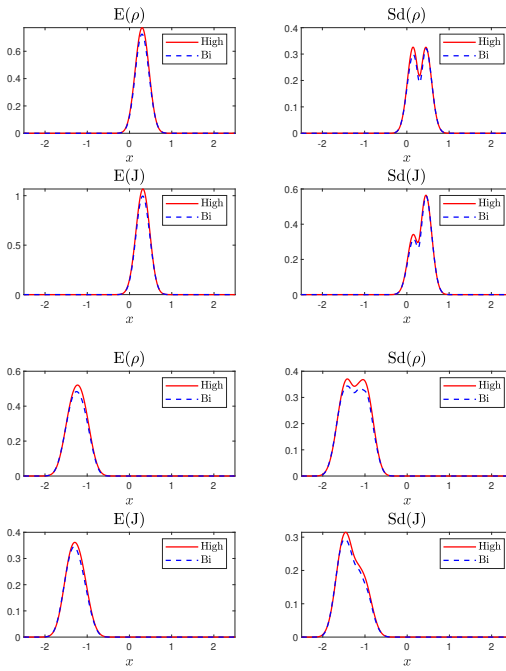


FIG. 8. Test 2. The mean and standard deviation of high- and bi-fidelity solutions ρ and J with $r = 25, \varepsilon = 1/32$ at different time, with $t = 1$ for the top two lines, and $t = 6$ for the bottom two lines.

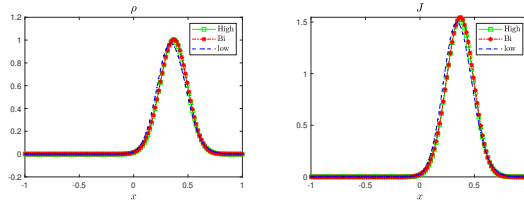


FIG. 9. Test 2. Comparison of the low-fidelity solution (FGA), high-fidelity solution (TSFP) and the corresponding bi-fidelity approximations with $r = 25, \varepsilon = 1/32, t = 1.0$ for a fixed z .

the mean and standard deviation of the bi-fidelity approximation of ρ and J match well with the high-fidelity solutions by using 25 high-fidelity runs. When $\varepsilon = 1/32$, the high-fidelity model (TSFP) costs approximately 7 times of the low-fidelity solver (FGA) with the final time $T = 6$ (the former takes 15.64 seconds while the latter takes 2.03 seconds for one single run). Therefore, a significant speedup is quite noticeable in this case. This shows the efficiency of our method to capture the long time behavior of the solution.

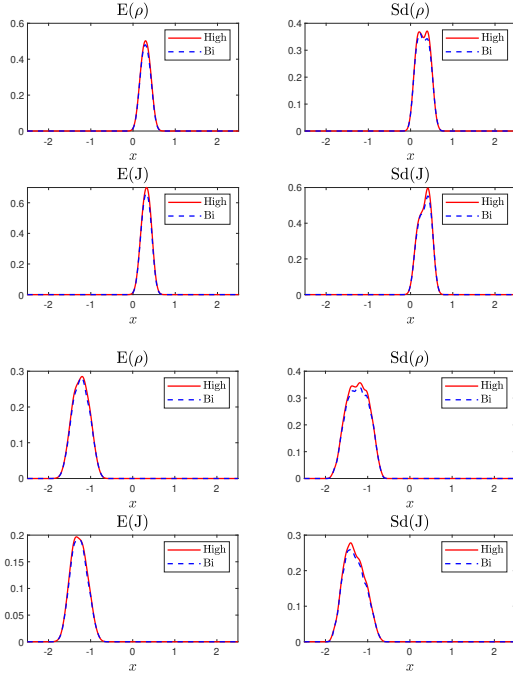


FIG. 10. *Test 2. The mean and standard deviation of high- and bi- fidelity solutions ρ and J with $r = 25, \varepsilon = 1/128$ at different time, with $t = 1$ for the top two lines, and $t = 6$ for the bottom two lines.*

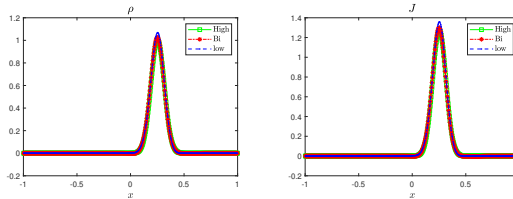


FIG. 11. *Test 2. Comparison of the low-fidelity solution (FGA), high-fidelity solution (TSFP) and the corresponding bi-fidelity approximations with $r = 25, \varepsilon = 1/128, t = 1.0$ for a fixed z .*

To further illustrate the performance of our bi-fidelity method, we compare the high-fidelity, low- and the corresponding bi-fidelity solutions (with $r = 25$) for a particular sample point z . One observes from Figure 9 ($\varepsilon = 1/32$) and Figure 11 ($\varepsilon = 1/128$) that the high- and bi-fidelity solutions match really well, whereas the low-fidelity solutions appear inaccurate at some points in the spatial domain.

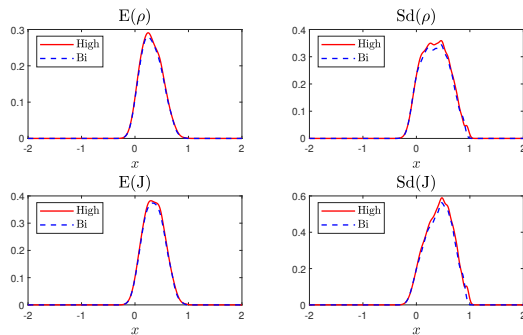


FIG. 12. *Test 2. The mean and standard deviation of high- and bi- fidelity solutions ρ and J with $r = 25, \varepsilon = 1/128$ at $t = 1$.*

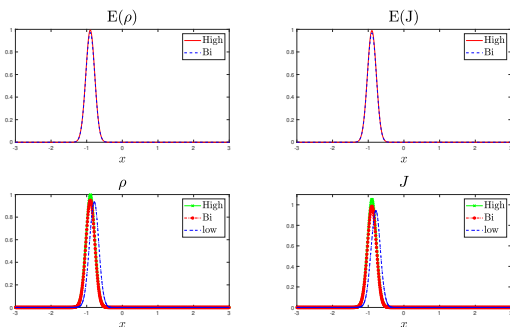


FIG. 13. *Expectation of high- and bi-fidelity solutions ρ and J with $r = 25, \varepsilon = 1/32$ (first row) and comparison of the low-fidelity solution (FGA), high-fidelity solution (TSFP) and the corresponding bi-fidelity approximations for a fixed z (second row).*

Finally, we add the randomness to the potential V apart from random initial parameters. Figure 12 shows the mean and standard deviation of high- and bi-fidelity solutions ρ and J at $r = 25, \varepsilon = 1/128, t = 1$ with a simple random potential $V(x, z) = x^2/2 + 0.5 \sum_{k=1}^{d_1} \frac{z_k}{2k}$ together with the random initial condition (4.2). Considering a more complex random potential $V(x, z) = \sum_{k=1}^{d_1} z_k \cdot (kx/10)^2$, Figure 13 ($\varepsilon = 1/32$) shows the expectation of high- and bi-fidelity solutions and comparison of the low-fidelity solution, high-fidelity solution and the corresponding bi-fidelity approximations for a particular sample point. The efficiency of our bi-fidelity method has been validated.

5. Conclusion. In this work, we study robust bi-fidelity and tri-fidelity method for the Schrödinger equation with random parameters. Different fidelity methods for solving the Schrödinger equation including the time-splitting Fourier pseudo-spectral (TSFP) method, the frozen Gaussian approximation (FGA), and level set (LS) method for the semi-classical limit of the Schrödinger equation are explored. Based on the error estimates for different numerical schemes, we conduct an error analysis of the bi-fidelity method. Moreover, we compare the bi-fidelity and tri-fidelity approximations, and give a summary on appropriate choices of low-fidelity models for general UQ problems. Extensive numerical examples have demonstrated the accuracy and efficiency of

our proposed bi-fidelity and tri-fidelity method for solving the Schrödinger equation with random inputs. In future work, we plan to investigate the error analysis for the multi-fidelity method and develop efficient multi-fidelity solvers for the Schrödinger equation with high-dimensional random parameters.

Acknowledgement. L. Liu acknowledges the support by National Key R&D Program of China (2021YFA1001200), Ministry of Science and Technology in China, Early Career Scheme (24301021) and General Research Fund (14303022 & 14301423) funded by Research Grants Council of Hong Kong from 2021-2023. Y. Lin was partially supported by National Natural Science Foundation of China (12201404) and China Postdoctoral Science Foundation (2021TQ0203). The computations in this paper were run on the Siyuan-1 cluster supported by the Center for High Performance Computing at Shanghai Jiao Tong University. We thank Prof. Shi Jin for his helpful discussions on improving our manuscript.

Appendix A. Proof of Lemma 3.4. Define

$$Y_N := \text{span} \left\{ e^{i\mu_l(x-a)}, x \in \bar{\Omega}, l \in \mathcal{T}_N \right\}, \mathcal{T}_N = \left\{ l \mid l = -\frac{N}{2}, \dots, \frac{N}{2} - 1 \right\},$$

where $\mu_l = \frac{2\pi l}{b-a}$. Let P_N be the standard L^2 -projection operator onto Y_N , and I_N be the trigonometric interpolation operator [26], i.e.,

$$P_N u = \sum_{l \in \mathcal{T}_N} \hat{u}_l e^{i\mu_l(x-a)}, \quad I_N u = \sum_{l \in \mathcal{T}_N} \tilde{u}_l e^{i\mu_l(x-a)}, \quad x \in \bar{\Omega},$$

where $\hat{u}_l = \frac{1}{b-a} \int_a^b u(x) e^{-i\mu_l(x-a)} dx$, $\tilde{u}_l = \frac{1}{N} \sum_{j=0}^{N-1} u(x_j) e^{-i\mu_l(x_j-a)}$, $l \in \mathcal{T}_N$. Since

$$I_N \psi^n - \psi(t_n) = I_N \psi^n - P_N(\psi(t_n)) + P_N(\psi(t_n)) - \psi(t_n),$$

under Assumption 3.3, the standard Fourier projection properties [26, 4] yield

$$(A.1) \quad \|I_N \psi^n - \psi(t_n)\|_{L^2} \leq \|I_N \psi^n - P_N(\psi(t_n))\|_{L^2} + C_1 h^m, .$$

Consider the error function e^n at t_n as $e^n := e^n(x) = I_N \psi^n - P_N \psi(t_n)$ ($n \geq 1$), and $\|e^0\|_{L^2} \leq C_2 h^m$ implied by the standard projection and interpolation results. We can write the error function e^n as

$$(A.2) \quad e^{n+1} = I_N \psi^{n+1} - P_N \mathcal{S}_\tau(P_N \psi(t_n)) + \mathcal{E}^n,$$

with the local truncation error $\mathcal{E}^n := \mathcal{E}^n(x) = P_N \mathcal{S}_\tau(P_N \psi(t_n)) - P_N \psi(t_{n+1})$. Here \mathcal{S}_τ is defined by

$$\mathcal{S}_\tau(P_N \psi(t_n)) = e^{i\frac{\varepsilon}{2}\frac{\tau}{2}\Delta} e^{-i\frac{\tau}{\varepsilon}V(x)} e^{i\frac{\varepsilon}{2}\frac{\tau}{2}\Delta} P_N \psi(t_n), \quad x \in \bar{\Omega}.$$

Taking the L^2 -norm on both sides of (A.2), one has

$$\|e^{n+1}\|_{L^2} \leq \|I_N \psi^{n+1} - P_N \mathcal{S}_\tau(P_N \psi(t_n))\|_{L^2} + \|\mathcal{E}^n\|_{L^2}.$$

Step 1. Estimate for $\|I_N \psi^{n+1} - P_N \mathcal{S}_\tau(P_N \psi(t_n))\|$. The fully discrete scheme (2.9) can be written as

$$\begin{aligned} I_N \psi^{n+1} &= e^{i\frac{\varepsilon}{2}\frac{\tau}{2}\Delta} \left(I_N \psi^{(**)} \right), I_N \left(\psi^{(**)} \right) = I_N \left(e^{-i\frac{\tau}{\varepsilon}V(x)} \psi^{(*)} \right), I_N \psi^{(*)} = e^{i\frac{\varepsilon}{2}\frac{\tau}{2}\Delta} I_N \psi^n, \\ P_N \left(\mathcal{S}_\tau \left(\psi(t_n) \right) \right) &= e^{i\frac{\varepsilon}{2}\frac{\tau}{2}\Delta} \left(P_N \psi^{(**)} \right), \psi^{(**)} = e^{-i\frac{\tau}{\varepsilon}V(x)} \psi^{(*)}, \psi^{(*)} = e^{i\frac{\varepsilon}{2}\frac{\tau}{2}\Delta} P_N \psi(t_n). \end{aligned}$$

Since I_N and P_N are identical on Y_N and $e^{i\frac{\varepsilon}{2}\frac{\tau}{\varepsilon}\Delta}$ preserves the H^k -norm ($k \geq 0$), using Taylor expansion $e^{-i\frac{\tau}{\varepsilon}V(x)} = 1 - i\frac{\tau}{\varepsilon}V(x) \int_0^1 e^{-i\theta\frac{\tau}{\varepsilon}V(x)} d\theta$ and Assumption 3.3, one has

$$(A.3) \quad \begin{aligned} & \left\| I_N \psi^{n+1} - P_N \mathcal{S}_\tau (P_N \psi(t_n)) \right\|_{L^2} \\ &= \left\| I_N \psi^{(**)} - P_N \psi^{(**)} \right\|_{L^2} \\ &\leq \left\| I_N \psi^{(**)} - I_N \psi^{(*)} \right\|_{L^2} + \left\| I_N \psi^{(*)} - P_N \psi^{(*)} \right\|_{L^2}, \end{aligned}$$

and

$$(A.4) \quad \begin{aligned} \left\| P_N \psi^{(*)} - I_N \psi^{(*)} \right\|_{L^2} &= \left\| \frac{\tau}{\varepsilon} (P_N - I_N) \left(V(x) \int_0^1 e^{-i\theta\frac{\tau}{\varepsilon}V(x)} d\theta \psi^{(*)} \right) \right\|_{L^2} \\ &\leq C_3 \frac{\tau}{\varepsilon} h^m, \end{aligned}$$

where C_3 is obtained from Fourier interpolation and projection properties together with $\left\| V(x) \int_0^1 e^{-i\theta\frac{\tau}{\varepsilon}V(x)} d\theta \psi^{(*)} \right\|_{L^2} \lesssim \|V\|_{L^2} \|\psi(t_n)\|_{L^2}$. In addition, by direct computation and Parseval's identity, we can derive

$$(A.5) \quad \begin{aligned} \left\| I_N \psi^{(**)} - I_N \psi^{(*)} \right\|_{L^2} &= \sqrt{h \sum_{j=0}^{N-1} \left| \psi_j^{(**)} - \psi_j^{(*)} \right|^2} = \sqrt{h \sum_{j=0}^{N-1} \left| \psi_j^{(1)} - \psi_j^{(*)} \right|^2} \\ &= \left\| I_N \psi^{(*)} - I_N \psi^{(*)} \right\|_{L^2} = \left\| I_N \psi^n - P_N \psi(t_n) \right\|_{L^2} = \|e^n\|_{L^2}. \end{aligned}$$

Combining (A.3), (A.4) and (A.5) together, we obtain

$$(A.6) \quad \begin{aligned} \left\| I_N \psi^{n+1} - P_N \mathcal{S}_\tau (P_N \psi(t_n)) \right\|_{L^2} &\leq \left\| I_N \psi^{(**)} - I_N \psi^{(*)} \right\|_{L^2} + \left\| I_N \psi^{(*)} - P_N \psi^{(*)} \right\|_{L^2} \\ &\leq \|e^n\|_{L^2} + C_3 \frac{\tau}{\varepsilon} h^m, \end{aligned}$$

Step 2. Estimate for $\|\mathcal{E}^n\|$. By the Taylor expansion for $e^{-i\frac{\tau}{\varepsilon}V}$, we have

$$(A.7) \quad \begin{aligned} P_N (\mathcal{S}_\tau (P_N \psi(t_n))) &= e^{i\frac{\varepsilon}{2}\tau\Delta} P_N \psi(t_n) - i\frac{\tau}{\varepsilon} P_N \left(e^{i\frac{\varepsilon}{2}\frac{\tau}{\varepsilon}\Delta} V e^{i\frac{\varepsilon}{2}\frac{\tau}{\varepsilon}\Delta} P_N \psi(t_n) \right) \\ &\quad - \frac{\tau^2}{\varepsilon^2} P_N \left(\int_0^1 (1-\theta) e^{i\frac{\varepsilon}{2}\frac{\tau}{\varepsilon}\Delta} e^{-i\frac{\tau}{\varepsilon}V} V^2 e^{i\frac{\varepsilon}{2}\frac{\tau}{\varepsilon}\Delta} P_N \psi(t_n) d\theta \right). \end{aligned}$$

By repeatedly using the Duhamel's principle, one can write

$$\begin{aligned} P_N \psi(t_{n+1}) &= P_N \left(e^{i\frac{\varepsilon}{2}\tau\Delta} \psi(t_n) \right) - i\frac{1}{\varepsilon} P_N \left(\int_0^\tau e^{i\frac{\varepsilon}{2}(\tau-s)\Delta} V e^{i\frac{\varepsilon}{2}s\Delta} \psi(t_n) ds \right) \\ &\quad - \frac{1}{\varepsilon^2} P_N \left(\int_0^\tau \int_0^s e^{i\frac{\varepsilon}{2}(\tau-s)\Delta} V e^{i\frac{\varepsilon}{2}(s-w)\Delta} V \psi(t_n + w) dw ds \right). \end{aligned}$$

Recall Assumption 3.3 and apply the Fourier projections,

$$(A.8) \quad \begin{aligned} P_N \psi(t_{n+1}) &= e^{i\frac{\varepsilon}{2}\tau\Delta} P_N \psi(t_n) - i\frac{1}{\varepsilon} \int_0^\tau P_N \left(e^{i\frac{\varepsilon}{2}(\tau-s)\Delta} V e^{i\frac{\varepsilon}{2}s\Delta} P_N \psi(t_n) \right) ds \\ &\quad - \frac{1}{\varepsilon^2} \int_0^\tau \int_0^s P_N \left(e^{i\frac{\varepsilon}{2}(\tau-s)\Delta} V e^{i\frac{\varepsilon}{2}(s-w)\Delta} V P_N \psi(t_n + w) \right) dw ds - r_h^n, \end{aligned}$$

with $\|r_h^n(x)\|_{L^2} \lesssim \frac{\tau}{\varepsilon} h^m$. Combining (A.7) and (A.8), the local truncation error of the TSFP (2.9) for the Schrödinger equation at time t_n can be written as [20]

$$(A.9) \quad \begin{aligned} \mathcal{E}^n &:= P_N \mathcal{S}_\tau(P_N \psi(t_n)) - P_N \psi(t_{n+1}) \\ &= P_N \mathcal{F}(P_N \psi(t_n)) - \frac{\tau^2}{2\varepsilon^2} B^n\left(\frac{\tau}{2}, \frac{\tau}{2}\right) + \frac{r_1^n}{\varepsilon^2} + \frac{1}{\varepsilon^2} \int_0^\tau \int_0^s B^n(s, w) dw ds + \frac{r_2^n}{\varepsilon^2} + r_h^n, \end{aligned}$$

where

$$\begin{aligned} \mathcal{F}(P_N \psi(t_n)) &= -i \frac{\tau}{\varepsilon} f^n\left(\frac{\tau}{2}\right) + i \frac{1}{\varepsilon} \int_0^\tau f^n(s) ds, \quad f^n(s) = e^{i\frac{\varepsilon}{2}(\tau-s)\Delta} V e^{i\frac{\varepsilon}{2}s\Delta} P_N \psi(t_n) \\ B^n(s, w) &= P_N \left(e^{i\frac{\varepsilon}{2}(\tau-s)\Delta} V e^{i\frac{\varepsilon}{2}(s-w)\Delta} V e^{i\frac{\varepsilon}{2}w\Delta} P_N \psi(t_n) \right), \\ r_1^n &= -\tau^2 \int_0^1 (1-\theta) P_N \left(e^{i\frac{\varepsilon}{2}\frac{\tau}{2}\Delta} (e^{-i\theta\frac{\tau}{\varepsilon}V} - 1) V^2 e^{i\frac{\varepsilon}{2}\frac{\tau}{2}\Delta} P_N \psi(t_n) \right) d\theta, \\ r_2^n &= \int_0^\tau \int_0^s \left(P_N \left(e^{i\frac{\varepsilon}{2}(\tau-s)\Delta} V e^{i\frac{\varepsilon}{2}(s-w)\Delta} V P_N \psi(t_n + w) \right) - B^n(s, w) \right) dw ds. \end{aligned}$$

The first term in (A.9) can be estimated by the midpoint quadrature rule as [20]

$$\|\mathcal{F}(P_N \psi(t_n))\|_{L^2} \lesssim \frac{\tau^3}{\varepsilon} \|[\Delta, [\Delta, V]] P_N \psi(t_n)\|_{L^2} \lesssim \frac{\tau^3}{\varepsilon} \|V\|_{H^4} \|\psi(t_n)\|_{H^2},$$

where $[\Delta, [\Delta, V]]$ is the double commutator. One has

$$\|r_1^n\|_{L^2} \lesssim \frac{\tau^3}{\varepsilon} \|V\|_{L^2}^3 \|\psi(t_n)\|_{L^2} \lesssim \frac{\tau^3}{\varepsilon}.$$

since $e^{i\frac{\varepsilon}{2}\frac{\tau}{2}\Delta}$ preserves the L^2 -norm and $\|(e^{-i\theta\frac{\tau}{\varepsilon}V} - 1) V^2\|_{L^2} \lesssim \frac{\tau}{\varepsilon} \theta \|V\|_{L^2}^3$. The following estimates are standard [20],

$$\begin{aligned} \|r_2^n\|_{L^2} &\lesssim \frac{\tau^3}{\varepsilon} \|V\|_{L^2}^2 \|V\psi(\cdot)\|_{L^\infty([0, \tau]; L^2)} \lesssim \frac{\tau^3}{\varepsilon}, \\ \left\| -\frac{\tau^2}{2} B\left(\frac{\tau}{2}, \frac{\tau}{2}\right) + \int_0^\tau \int_0^s B(s, w) dw ds \right\|_{L^2} &\lesssim \tau^3 \|V\|_{H^2}^2 \|\psi(t_n)\|_{H^2} \lesssim \frac{\tau^3}{\varepsilon^2}. \end{aligned}$$

Combining the above estimates together, the following L^2 -estimate

$$(A.10) \quad \|\mathcal{E}^n\|_{L^2} \lesssim \frac{\tau^3}{\varepsilon^4} + \frac{\tau}{\varepsilon} h^m$$

holds for $m \geq 2$.

Finally, combining (A.6) and (A.10), one obtains

$$\begin{aligned} \|e^{n+1}\|_{L^2} &\leq \|I_N \psi^{n+1} - P_N \mathcal{S}_\tau(P_N \psi(t_n))\|_{L^2} + \|\mathcal{E}^n\|_{L^2} \\ &\leq \|I_N \psi^{(**)} - I_N \psi^{(*)}\|_{L^2} + \|I_N \psi^{(*)} - P_N \psi^{(*)}\|_{L^2} + \|\mathcal{E}^n\|_{L^2} \\ &\leq \|e^n\|_{L^2} + C_4 \left(\frac{\tau}{\varepsilon} h^m + \frac{\tau^3}{\varepsilon^4} \right). \end{aligned}$$

Together with $\|e^0\|_{L^2} \leq C_2 h^m$, the following estimate

$$(A.11) \quad \|e^{n+1}\|_{L^2} \leq C_4 \frac{t_{n+1}}{\varepsilon} \left(h^m + \frac{\tau^2}{\varepsilon^3} \right) + C_2 h^m, \quad 0 \leq n \leq \frac{T}{\tau} - 1,$$

holds. From (A.1) and (A.11), the estimate can be derived

$$\|I_N \psi^n - \psi(t_n)\|_{L^2} \leq C_0 G_m \frac{T}{\varepsilon} \left(h^m + \frac{\tau^2}{\varepsilon^3} \right).$$

Here $C_0 = \max\{C_1 + C_2, C_4\}$ is independent of $\varepsilon, h, \tau, n, m$, and G_m is independent of ε, h, τ and only depends on V and ψ . This completes the proof of L^2 -estimate (3.3).

Appendix B. Proof of (3.10). By the definition of projection onto $\mathcal{U}_j^L(\gamma_K)$ for each $\mathbf{U}_j^L(z) (j = 1, 2)$ given in (2.1),

$$\left(\mathcal{P}_{\mathcal{U}_j^L(\gamma_K)} \left[\mathbf{U}_j^L(z) \right] \right)^2 = \sum_{k,s=1}^K c_k(z) c_s(z) \mathbf{U}_j^L(z_k) \mathbf{U}_j^L(z_s),$$

thus

$$\begin{aligned} \int_{\Omega} \left(\mathcal{P}_{\mathcal{U}_j^L(\gamma_K)} \left[\mathbf{U}_j^L(z) \right] \right)^2 dx &= \sum_{k,s=1}^K c_k(z) c_s(z) \int_{\Omega} \mathbf{U}_j^L(z_k) \mathbf{U}_j^L(z_s) dx \\ &:= \mathbf{c}_j^T \mathbf{G}_j^L \mathbf{c}_j \geq \lambda_{j,0} \|\mathbf{c}_j\|^2, \end{aligned}$$

where \mathbf{G}_j^L is the Gramian matrix of $\mathcal{U}_j^L(\gamma_K)$ defined in (2.3) (where $\langle \cdot, \cdot \rangle$ applies to L_x^2 here) and $\lambda_{j,0} > 0$ is its minimum eigenvalue. Since for all z ,

$$\int_{\Omega} \left(\mathcal{P}_{\mathcal{U}_j^L(\gamma_K)} \left[\mathbf{U}_j^L(z) \right] \right)^2 dx \leq \int_{\Omega} \left[\mathbf{U}_j^L(z) \right]^2 dx, \quad j = 1, 2,$$

then

$$(B.1) \quad \|\mathbf{c}_j\| \leq \frac{1}{\sqrt{\lambda_{j,0}}} \left(\int_{\Omega} \left(\mathcal{P}_{\mathcal{U}_j^L(\gamma_K)} \left[\mathbf{U}_j^L(z) \right] \right)^2 dx \right)^{1/2} \leq \frac{1}{\sqrt{\lambda_{j,0}}} \left\| \mathbf{U}_j^L(z) \right\|_0,$$

for all z . Thus

$$\|\|\mathbf{c}_j\|\|_{L_z^2} \leq \frac{1}{\sqrt{\lambda_{j,0}}} \left\| \mathbf{U}_j^L(z) \right\|_{L_x^2 L_z^2}.$$

Since \sqrt{x} is a monotone function,

$$\|\|\mathbf{c}_j\|\|_{L_z^2} = \left(\sum_{k=1}^K \|c_k(z)\|_{L_z^2}^2 \right)^{1/2}.$$

By the regularity of \mathbf{U}_j^L and the assumption that the volume of Ω is bounded, (B.1) implies (3.10).

Appendix C. Numerical observation on the bound of $\|\rho_z\|_{L^2}$. Regarding Test 1 in our numerical examples, we investigate ρ and ρ_z and study their behaviours in the random space by plotting some quantities in Figure 14. Based on these observations, we conclude that the L_z^2 norm of ρ_z is bounded by $O(1/\varepsilon)$.

If one considers the WKB ansatz that solves the Schrödinger equation (1.1), i.e.,

$$(C.1) \quad \psi^\varepsilon(t, x, z) = \sqrt{\rho^\varepsilon(t, x, z)} \exp\left(\frac{i}{\varepsilon} S^\varepsilon(t, x, z)\right),$$

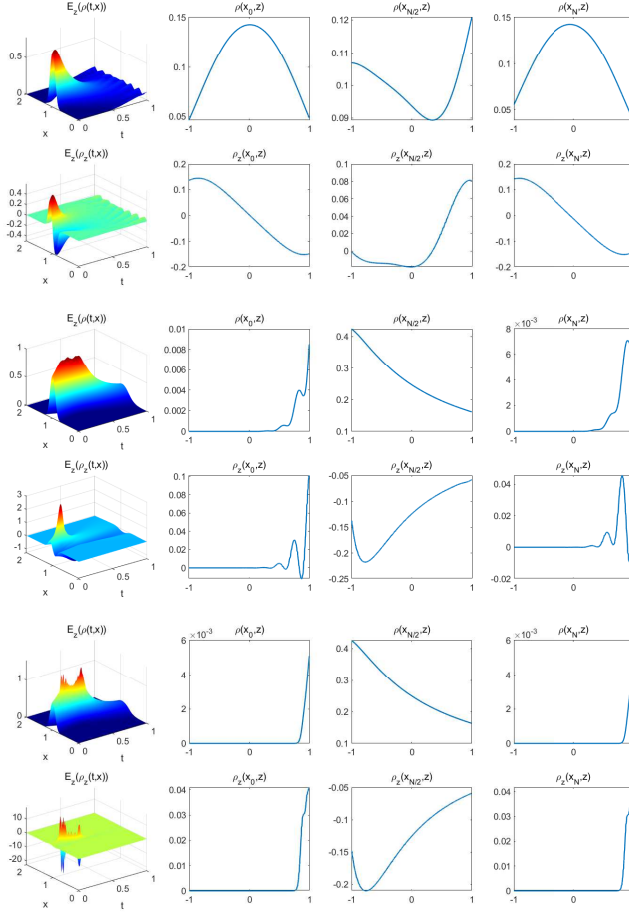


FIG. 14. *Test 1. The mean of ρ and ρ_z (first column) and the behavior of ρ and ρ_z in the random space at three different points $x_0, x_{N/2}, x_N$ (second to fourth columns) at $T = 1$. The first two rows are the results for $\varepsilon = 0.1$; the medium two rows are for $\varepsilon = 0.01$; and the last two rows are for $\varepsilon = 0.001$.*

where $\rho^\varepsilon = |\psi^\varepsilon|^2$ and S^ε are the density and phase function respectively. Inserting (C.1) into the Schrödinger equation (1.1) and separating the real and imaginary parts give

$$\begin{aligned} \rho_t^\varepsilon + \partial_x (\rho^\varepsilon S_x^\varepsilon) &= 0, \\ S_t^\varepsilon + \frac{1}{2} |S_x^\varepsilon|^2 + V^\varepsilon(x, z) &= \frac{\varepsilon^2}{2} \frac{(\sqrt{\rho^\varepsilon})_{xx}}{\sqrt{\rho^\varepsilon}}. \end{aligned}$$

Since this coupled system is nonlinear, even just for the WKB form of the wave solution, a rigorous analysis on studying the regularity of ρ in the random space is non-trivial, thus we consider it as a future work and only give findings based on our numerical observations.

REFERENCES

- [1] I. BABUŠKA, F. NOBILE, AND R. TEMPONE, *A stochastic collocation method for elliptic partial differential equations with random input data*, SIAM Rev., 52 (2010), pp. 317–355.
- [2] G. BAL, A. FANNJIANG, G. PAPANICOLAOU, AND L. RYZHIK, *Radiative transport in a periodic structure*, J. Statist. Phys., 95 (1999), pp. 479–494.
- [3] W. BAO AND Y. CAI, *Uniform and optimal error estimates of an exponential wave integrator sine pseudospectral method for the nonlinear schrödinger equation with wave operator*, SIAM J. Numer. Anal., 52 (2014), pp. 1103–1127.
- [4] W. BAO, Y. CAI, AND Y. FENG, *Improved uniform error bounds of the time-splitting methods for the long-time (nonlinear) Schrödinger equation*, Math. Comp., 92 (2023), pp. 1109–1139.
- [5] W. BAO, S. JIN, AND P. A. MARKOWICH, *On time-splitting spectral approximations for the schrödinger equation in the semiclassical regime*, J. Comput. Phys., 175 (2002), pp. 487–524.
- [6] M. BIERI AND C. SCHWAB, *Sparse high order FEM for elliptic sPDEs*, Comput. Methods Appl. Mech. Engrg., 198 (2009), pp. 1149–1170.
- [7] A. COHEN AND R. DEVORE, *Approximation of high-dimensional parametric PDEs*, Acta Numer., 24 (2015), pp. 1–159.
- [8] R. DEVORE, G. PETROVA, AND P. WOJTASZCZYK, *Greedy algorithms for reduced bases in Banach spaces*, Constr. Approx., 37 (2013), pp. 455–466.
- [9] B. ENGQUIST AND O. RUNBORG, *Computational high frequency wave propagation*, Acta Numer., 12 (2003), pp. 181–266.
- [10] I. M. GAMBA, S. JIN, AND L. LIU, *Error estimate of a bifidelity method for kinetic equations with random parameters and multiple scales*, Int. J. Uncertain. Quan., 11 (2021), pp. 57–75.
- [11] P. GÉRARD, P. A. MARKOWICH, N. J. MAUSER, AND F. POUPAUD, *Homogenization limits and Wigner transforms*, Comm. Pure Appl. Math., 53 (2000), pp. 280–281.
- [12] S. JIN, H. LIU, S. OSHER, AND Y.-H. R. TSAI, *Computing multivalued physical observables for the semiclassical limit of the schrödinger equation*, J. Comput. Phys., 205 (2005), pp. 222–241.
- [13] S. JIN, L. LIU, G. RUSSO, AND Z. ZHOU, *Gaussian wave packet transform based numerical scheme for the semi-classical schrödinger equation with random inputs*, J. Comput. Phys., 401 (2020), p. 109015.
- [14] S. JIN, P. MARKOWICH, AND C. SPARBER, *Mathematical and computational methods for semiclassical schrödinger equations*, Acta Numer., 20 (2011), pp. 121–209.
- [15] S. JIN, P. MARKOWICH, AND C. SPARBER, *Mathematical and computational methods for semiclassical Schrödinger equations*, Acta Numer., 20 (2011), pp. 121–209.
- [16] S. JIN, H. WU, AND X. YANG, *Gaussian beam methods for the schrodinger equation in the semiclassical regime: Lagrangian and eulerian formulations*, Commun. Math. Sci., 6 (2008), pp. 995–1020.
- [17] C. LASSER AND C. LUBICH, *Computing quantum dynamics in the semiclassical regime*, Acta Numer., 29 (2020), pp. 229–401.
- [18] Y. LIN AND S. JIN, *Error estimates of a bi-fidelity method for a multi-phase navier-stokes-vaslov-fokker-planck system with random inputs*, 2024.
- [19] J. LU AND Z. ZHOU, *Frozen gaussian approximation with surface hopping for mixed quantum-classical dynamics: A mathematical justification of fewest switches surface hopping algorithms*, Math. Comput., 87 (2017), pp. 2189–2232.
- [20] C. LUBICH, *On splitting methods for schrödinger-poisson and cubic nonlinear schrödinger equations*, Math. Comput., 77 (2008), pp. 2141–2153.
- [21] B. MIAO, G. RUSSO, AND Z. ZHOU, *A novel spectral method for the semiclassical schrödinger equation based on the gaussian wave-packet transform*, IMA J. Numer. Anal., 43 (2023), pp. 1221–1261.
- [22] A. NARAYAN, C. GITTELSON, AND D. XIU, *A stochastic collocation algorithm with multifidelity models*, SIAM J. Sci. Comput., 36 (2014), pp. A495–A521.
- [23] A. NARAYAN AND D. XIU, *Stochastic collocation methods on unstructured grids in high dimensions via interpolation*, SIAM J. Sci. Comput., 34 (2012), pp. A1729–A1752.
- [24] F. NOBILE, R. TEMPONE, AND C. G. WEBSTER, *A sparse grid stochastic collocation method for partial differential equations with random input data*, SIAM J. Numer. Anal., 46 (2008), pp. 2309–2345.
- [25] L. PARESCHI, *An introduction to uncertainty quantification for kinetic equations and related problems*, vol. 25 of SEMA SIMAI Springer Ser., Springer, Cham, 2021, pp. 141–181.
- [26] J. SHEN, T. TANG, AND L.-L. WANG, *Spectral methods: algorithms, analysis and applications*, vol. 41, Springer Science & Business Media, 2011.
- [27] T. SWART AND V. ROUSSE, *A mathematical justification for the Herman-Kluk propagator*,

- Commun. Math. Phys., 286 (2009), pp. 725–750.
- [28] D. XIU, *Efficient collocational approach for parametric uncertainty analysis*, Commun. Comput. Phys., 2 (2007), pp. 293–309.
 - [29] D. XIU AND J. S. HESTHAVEN, *High-order collocation methods for differential equations with random inputs*, SIAM J. Sci. Comput., 27 (2005), pp. 1118–1139.
 - [30] Z. ZHOU, *Numerical approximation of the schrödinger equation with the electromagnetic field by the hagedorn wave packets*, J. Comput. Phys., 272 (2014), pp. 386–407.
 - [31] X. ZHU, A. NARAYAN, AND D. XIU, *Computational aspects of stochastic collocation with multifidelity models*, SIAM/ASA J. Uncertain. Quantif., 2 (2014), pp. 444–463.